



Hierarchical shape optimization for complex shell structures considering global and local shape perturbations

Chang Liu^{1,3} · Yanbo Ren¹ · Shixin Zhao¹ · Xianglong Cao¹ · Yilin Guo¹ · Wendong Huo¹ · Xu Guo^{1,2,3}

Received: 4 February 2025 / Revised: 15 August 2025 / Accepted: 21 August 2025 / Published online: 24 September 2025
© The Author(s), under exclusive licence to Springer-Verlag GmbH Germany, part of Springer Nature 2025

Abstract

Shell structures effectively resist external loads due to their characteristic geometric shapes. Shape optimization can further enhance the mechanical performance of shell structures while preserving structural topology. This paper proposes a novel shape design concept based on the hierarchical shape representation. We use a NURBS network to control the global surface geometry and explicit spline components to capture local geometric features. The hierarchical representation enables coordinated control of both global shape and local details using a small number of design variables, thereby reducing the computational burden of the optimization problem. During the optimization process, the hierarchical shape variations are implemented by applying global and local perturbations to the discrete triangular mesh of the shell surface. By employing the computational conformal mapping technique, we obtain the parametric domain of the initial model, in which the hierarchical perturbations are constructed. The surface cutting operation and the multi-patch stitching scheme are employed to preprocess the geometry for extension to complex shell structures. Numerical examples are provided to validate the effectiveness, efficiency, and generality of the proposed hierarchical shape design method for complex shell structures.

Keywords Shell structures · Shape optimization · Moving morphable components (MMC) · Computational conformal mapping (CCM)

1 Introduction

Shell structures can effectively bear external loads based on their geometric shape and have been widely applied in both nature and engineering practice (Chapelle and Bathe

Responsible Editor: Eddie Wadbro.

ICTAM 2024 - The centennial of ICTAM Guest Editors: J. Alexandersen, A.M. Aragón, X.S. Zhang, E. Lund, E. Wadbro, J. Kook.

✉ Wendong Huo
huowd@mail.dlut.edu.cn

¹ State Key Laboratory of Structural Analysis, Optimization and CAE Software for Industrial Equipment, Department of Engineering Mechanics, International Research Center for Computational Mechanics, Dalian University of Technology, Dalian 116023, People's Republic of China

² Dalian Institute of Industrial Software, No. 1 Huoju Road, High-Tech Industrial Park, Dalian 116085, People's Republic of China

³ Ningbo Institute of Dalian University of Technology, Ningbo 315016, People's Republic of China

2011). Their superior span-to-thickness ratio and stiffness-to-weight ratio enable them to play a critical role in various fields such as architecture (Rian et al. 2018), shipbuilding (Yu et al. 2015), aerospace engineering (Talebitooti and Zarastvand 2018), and the automotive industry (Lee et al. 2003). Shape optimization of shell structures can enhance structural performance by modifying the outer profile while preserving the structural topology. This approach has significant application value in typical thin-walled structures such as aircraft skins and pipeline shells, and has attracted extensive attention from researchers. From the perspective of implementation methods, shape optimization of shell structures can be broadly categorized into two main types: CAD-based methods and node-based methods (Samareh 2001).

CAD-based methods typically describe the middle surface of shell structures using spline tools commonly employed in geometric modeling, where the design variables correspond to the geometric parameters defining the splines. The development of various spline tools has greatly advanced this approach. Surfaces such as Coons surfaces (Afonso and Hinton 1995; Falco et al. 2004), Bézier surfaces (Wang et al. 2003), B-spline surfaces (Ansola et al.

2002a, b; Suarez Espinoza et al. 2012), and NURBS surfaces (Espath et al. 2011; Vu Bac et al. 2018) have been employed to describe shell shape, enabling both accurate representation and efficient optimization of shell structures. Compared to Coons and Bézier surfaces, B-spline surfaces successfully address the issue of local control by introducing knot vectors, enabling finer model adjustments. Building on this, NURBS (Non-Uniform Rational B-Splines) surfaces (Piegl and Tiller 2012) further incorporate weights to rationalize the formulation, providing a unified mathematical framework for representing both regular and free-form surfaces, thereby significantly enhancing geometric representation capabilities. With their high flexibility and degrees of freedom, B-spline and NURBS representations have become the primary modeling tools in CAD-based shape optimization methods for shell structures. CAD-based methods leverage the inherent smoothness of spline representations to control structural shapes with a relatively small number of design variables, resulting in smooth optimized designs. However, these methods often suffer from the computational burden of remeshing at each iteration. Isogeometric Analysis (IGA, Hughes et al. 2005) employs the same basis functions used in geometric modeling, allowing the design model and analysis model to share a common parameterization. This approach effectively reduces the frequent communication and remeshing between the design and analysis models, thereby significantly improving computational efficiency. Combining IGA with shape optimization is highly attractive and has been widely applied in structural and fluid dynamic shape optimization (Wall et al. 2008; Qian 2010; Nørtoft and Gravesen 2013; Park et al. 2013; Wang et al. 2018). In addition, Kang and Youn (2015, 2016) and Chasapi et al. (2024) achieved shape optimization of shell structures with complex boundaries or holes by combining IGA with trimmed surface analysis (TSA) techniques, ensuring smooth geometric transitions along the trimmed boundaries. However, due to the lack of local refinement capability in the tensor-product spline spaces underlying isogeometric analysis, traditional spline formulations offer limited flexibility in controlling geometric details, which may lead to a certain dependence of the optimization outcomes on the initial shape. As the geometric complexity of shell structures increases, the difficulty of spline-based parameterization rises significantly, thereby limiting the further application of this technique in shape optimization of complex surface structures (Hirschler et al. 2019).

In contrast, node-based methods (also known as CAD-free, parameter-free, or grid-based) offer an alternative parameterization for shape optimization. These methods are constructed directly on the finite element discretized mesh of the shell structure, with design variables defined as the nodal coordinates or their perturbations, thereby providing greater flexibility in the optimization process. Although this

method provides a large design space, the substantial number of design variables may reduce the overall optimization efficiency. In addition, the optimized shapes can sometimes exhibit non-smooth or discontinuous geometries, which may pose challenges for direct application in engineering practice. Therefore, regularization techniques are commonly employed in shape and topology optimization to improve the smoothness of the design. Among these, filtering methods, often referred to as smoothing techniques, are the most widely used and can generally be categorized into implicit and explicit types. Implicit filtering generates smooth designs by solving an elliptic partial differential equation. Representative methods include the traction method, also known as the H^1 gradient method (Azegami and Wu 1996), Sobolev smoothing (Jameson and Vassberg 2000), and the enhanced traction method (Azegami and Takeuchi 2006). The work by Swartz et al. (2023) provides a comprehensive overview of implicit filtering techniques, greatly facilitating researchers' understanding of these methods. Explicit filtering achieves field smoothing through convolution with kernel functions. Originally introduced to address the checkerboard issue in topology optimization (Sigmund 1994), it has also been found effective in shape optimization (Le et al. 2011). Hojjat et al. (2014) and Bletzinger (2014) proposed the vertex-morphing method, demonstrating the application of explicit filtering techniques in shell shape optimization. In recent research, Schmözl et al. (2025) introduced a simultaneous optimization strategy for shell shape and thickness based on the vertex-morphing method. They conducted a comprehensive and detailed comparison with the approach proposed by Träff (2023), verifying the impact of the choice of filtering technique (implicit or explicit) on the results of combined optimization. Radtke et al. (2023) conducted an in-depth analysis of both explicit and implicit filtering techniques. Najian Asl and Bletzinger (2023) investigated convolution-based (explicit) and PDE-based (implicit) shape filtering methods, and introduced an implicit volumetric filtering approach that simultaneously controls boundary smoothness and preserves internal mesh quality during shape optimization. Although the application of various filtering techniques effectively improves the smoothness of optimization results, the additional operations introduced inevitably increase the computational time. Therefore, finding a balance between high flexibility and computational efficiency has become one of the key research focuses in the development of this method.

Overall, the two main existing shape parameterization methods each have their own advantages. To combine the strengths of both shape optimization approaches, this study proposes a novel shape parameterization method based on spline models from CAD-based methods and discrete meshes from node-based methods, enabling effective global shape representation. The method describes the shell middle

surface using the discrete triangular mesh and constructs a standardized parametric domain for the shape description through geometric preprocessing. A global shape network is built in the parametric domain using NURBS, and shell geometry variations are achieved by computing a perturbation height field applied to the discretized middle surface. In the proposed approach, variations of the shell middle surface shape are realized through normal perturbations of mesh nodes, while the design variables correspond to perturbation coefficients at the NURBS network control points. This parameterization method thus combines the advantages of CAD-based methods (few design variables and no need for filtering) with the geometric flexibility characteristic of node-based methods. In addition, we incorporate computational conformal mapping technique (Lui et al. 2013, 2014; Meng et al. 2016) as part of the geometric preprocessing to achieve a unified parameterization of the shell surface. By integrating the principles of computational conformal mapping (CCM) technique with the framework of the moving morphable components (MMC) method (Guo et al. 2014; Zhang et al. 2016), Huo et al. (2025) employed embedded spline components to optimize the surface topography of complex shell structures and investigated the influence of local shape variations on structural performance. Their study demonstrated that rich topographical adjustments on the shell surface can significantly enhance structural performance. However, in their approach, the global geometry of the structure remains fixed, and the optimization is limited to local shape modifications. To further explore the combined effects of global shape and local geometric details on structural performance, this study introduces local spline components into the proposed global shape optimization framework. This allows for simultaneous optimization of local features while the global geometry evolves, enabling a hierarchical shape optimization strategy that fully leverages the impact of shape variation on the mechanical performance of shell structures.

In the proposed method, the global and local shape optimizations of the shell structure are performed concurrently, with both types of design variables incorporated into a unified vector and updated simultaneously. The advantages of the proposed approach can be summarized as follows: First, the shell geometry is modeled using a mesh-based representation, which enhances adaptability to complex shapes. Shape modifications are realized by applying both global perturbations defined via NURBS and local perturbations described by embedded components directly to the mesh nodes, thereby eliminating the need for remeshing during the optimization process. Moreover, the use of local spline components within the MMC framework, together with the NURBS-based global shape network, significantly reduces the number of design variables, resulting in lower computational cost for the optimization problem.

The remainder of the article is organized as follows: Sect. 2 introduces the approach for realizing shape changes. In Sect. 3, the optimization problem is formulated with stiffness maximization as the objective function, accompanied by a detailed sensitivity analysis. Section 4 addresses key technical considerations relevant to the proposed approach and summarizes the overall design process. In Sect. 5, several representative numerical examples are presented to validate the effectiveness of the proposed method. Finally, the conclusions and future research directions are summarized in Sect. 6.

2 Shape description

This section outlines the implementation process of hierarchical shape description. For a shell structure to be designed, the middle surface of the shell is employed for structural modeling and its shape variations are realized through perturbations of the middle surface. We take the plane of a plate shell structure as an example to describe both the global and local perturbations, from which a hierarchical perturbation field is formulated. Subsequently, shape variations of complex surfaces are achieved by applying the hierarchical perturbations.

2.1 Global shape perturbation description

Taking the rectangular plane S shown in Fig. 1 as an example, a point $\mathbf{x} = (u, v)$ on the plane is perturbed along the unit normal vector $N(\mathbf{x})$ to a new position $\mathbf{x}^*(\mathbf{x})$ expressed as

$$\mathbf{x}^*(\mathbf{x}) = \mathbf{x} + h_S^g(\mathbf{x}) \cdot N(\mathbf{x}), \quad (1)$$

where $h_S^g(\mathbf{x})$ represents the global perturbation height field at point \mathbf{x} . Since the proposed method is designed for discrete mesh models, $N(\mathbf{x})$ is defined using discrete differential geometry (Taubin 1995). Inspired by CAD-based methods, Non-Uniform Rational B-Splines (Piegl and Tiller 2012) are introduced to construct the global shape network, thereby enabling the description of global shape perturbations. As shown in Fig. 2, the global perturbation height field $h_S^g(\mathbf{x})$ at point \mathbf{x} is defined as

$$h_S^g(\mathbf{x}) = \frac{\sum_{i=0}^n \sum_{j=0}^m N_{i,p}(u) N_{j,q}(v) \omega_{ij} h_{ij}}{\sum_{i=0}^n \sum_{j=0}^m N_{i,p}(u) N_{j,q}(v) \omega_{ij}}, \quad (2)$$

where $N_{i,p}$ and $N_{j,q}$ are basis functions in the u and v -directions, respectively. The parameters n and m denote the number of basis functions (corresponding to an $n \times m$ global shape network), and p and q represent the degrees of the basis functions ($p = q = 2$ in this study). The symbol h_{ij} represents the perturbation coefficient at the NURBS control

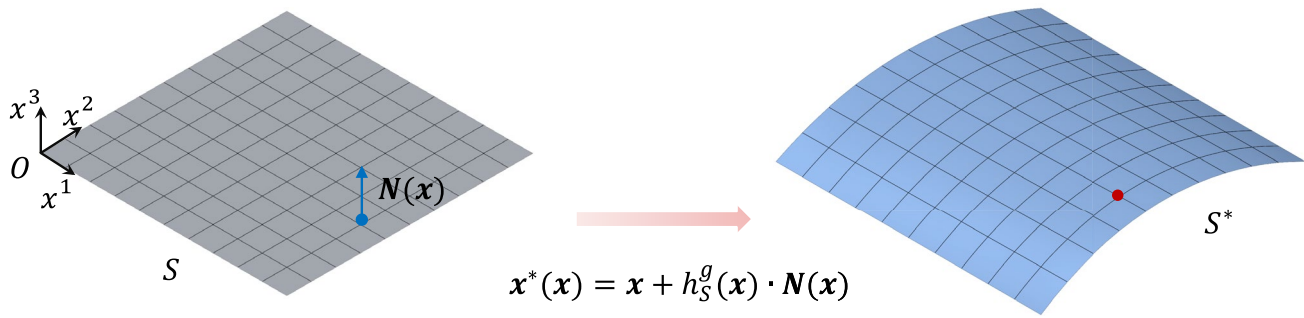


Fig. 1 Shape changes are achieved by perturbing the point on the surface. The perturbation direction follows the normal vector at each point of the initial surface

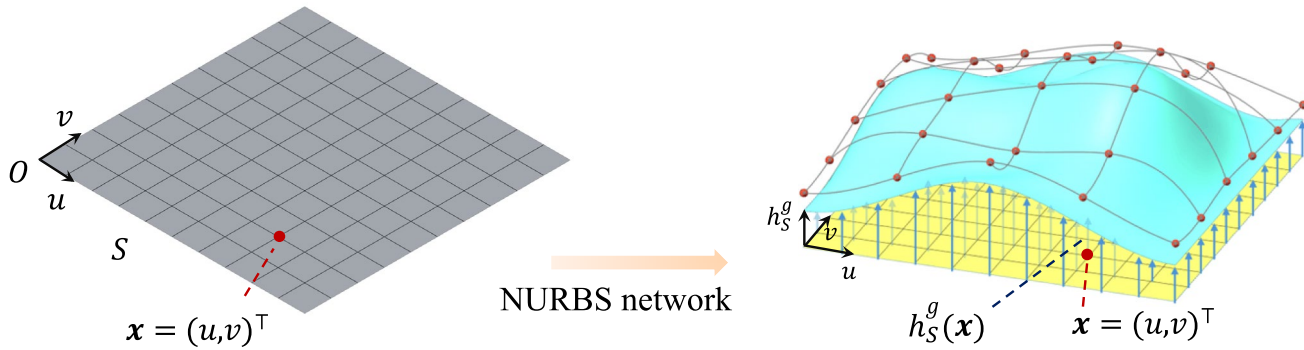


Fig. 2 Description of the global shape perturbation. Each point x on the initial surface S corresponds to a height value on the NURBS surface, which is regarded as the global perturbation height field $h_S^g(x)$

points, while ω_{ij} denotes the corresponding control point weights (set to $\omega_{ij} = 1$ in this study). The basis function $N_{i,p}(u)$ (and similarly $N_{j,q}(v)$) is calculated using the Cox–De Boor recursive formula (De Boor 1972)

$$N_{i,0}(u) = \begin{cases} 1, & \text{if } u_i \leq u \leq u_{i+1} \\ 0, & \text{otherwise,} \end{cases} \quad (3)$$

$$N_{i,p}(u) = \frac{u - u_i}{u_{i+p} - u_i} N_{i,p-1}(u) + \frac{u_{i+p+1} - u}{u_{i+p+1} - u_{i+1}} N_{i+1,p-1}(u),$$

where u_i denotes the i -th knot in the u -direction knot vector. The knot vectors in the u and v -directions are defined as

$$U = \{u_1, u_2, \dots, u_{n+p+1}\}, \quad (4)$$

$$V = \{v_1, v_2, \dots, v_{m+q+1}\}. \quad (5)$$

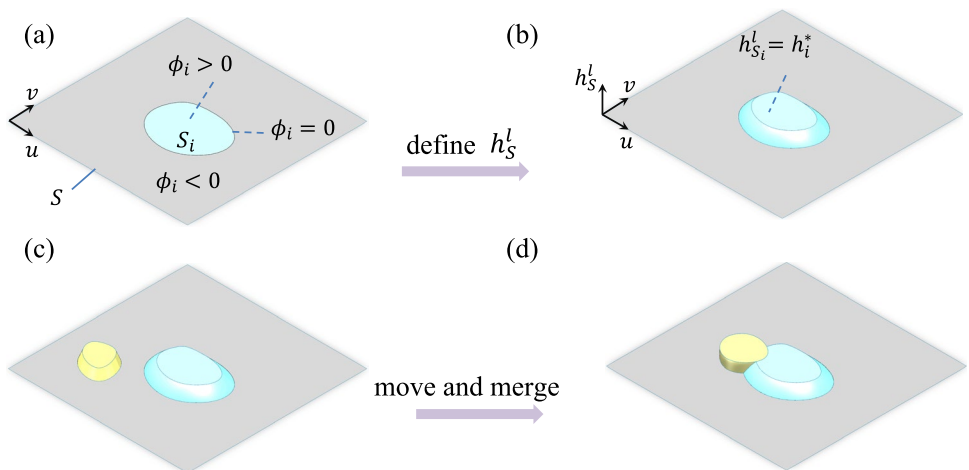
By introducing the NURBS-based shape network, global perturbations of the height field are achieved. The corresponding perturbation coefficients are used as design variables, denoted as $D^g = (h_{00}, \dots, h_{ij}, \dots, h_{nm})$.

2.2 Local shape perturbation description

In Eq. (1), the global shape variation of the plane S is achieved by defining a global perturbation height field $h_S^g(x)$. Similarly, in this subsection, we introduce the spline-based shape components developed in Huo et al. (2025) to define local shape perturbation height fields $h_S^l(x)$ for realizing localized shape variations. This approach is inspired by the concept of moving morphable components (Guo et al. 2014; Zhang et al. 2016) in explicit topology optimization frameworks, enabling an explicit representation of local shapes. As a result, the proposed method benefits from a reduced number of design variables, smooth and well-defined structural boundaries, and improved interpretability of the final designs. Specifically, the topology description function (TDF) is introduced to represent regions subjected to local shape perturbations. For the i -th local shape component on the rectangular plane S (Fig. 3a), its TDF is expressed as

$$\begin{cases} \phi_i(u, v) > 0, & \text{if } (u, v) \in S_i, \\ \phi_i(u, v) = 0, & \text{if } (u, v) \in \partial S_i, \\ \phi_i(u, v) < 0, & \text{if } (u, v) \in S \setminus (S_i \cup \partial S_i), \end{cases} \quad (6)$$

Fig. 3 Schematic illustration of local shape perturbation height field construction. **a** The TDF ϕ_i indicates the local shape perturbation domain. **b** Introduce the height variable h_i^* to represent the height field corresponding to the local perturbation domain. **c, d** represent the assembly process of multiple local shape components, forming the final local perturbation height field h_S^l , i.e. Eq. (8)



where S_i represents the region occupied by the i -th local shape component, and ∂S_i denotes its boundary. However, the TDF in Fig. 3a only indicates the region requiring local perturbation without reflecting the perturbation height field h_S^l . To address this, a height parameter is introduced to define the perturbation height field (Fig. 3b), which is expressed for the i -th component as

$$h_i^l(u, v) = h_i^* \cdot H(\phi_i(u, v)), \quad (7)$$

where h_i^* is the design variable, representing the height of the i -th local shape component, and $H(\cdot)$ is the regularized Heaviside function that maps values to the interval $[0, 1]$. After determining h_i^l for each local component, the local perturbation height field for the entire plane S can be expressed as (Fig. 3c, d)

$$h_S^l = \max(h_1^l, h_2^l, \dots, h_3^l, \dots, h_{nc}^l), \quad (8)$$

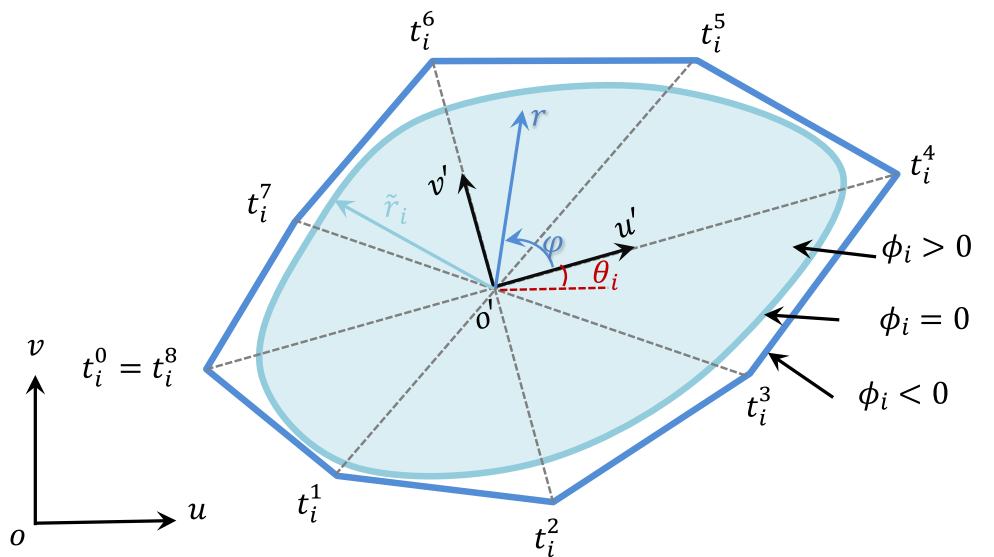
where nc is the number of local shape components in the design domain.

Next, the expression for the TDF $\phi_i(u, v)$ is formulated. To describe more intricate local shape changes, this study employs spline-based components to represent local shapes. To achieve this, the spline-based TDF $\phi_i(u, v)$ is defined as shown in Fig. 4. First, a local coordinate system (u', v') is established as

$$\begin{pmatrix} u' \\ v' \end{pmatrix} = \begin{bmatrix} \cos\theta_i & \sin\theta_i \\ -\sin\theta_i & \cos\theta_i \end{bmatrix} \begin{pmatrix} u - u_0^i \\ v - v_0^i \end{pmatrix}, \quad (9)$$

where u_0^i and v_0^i are the local coordinates of the i -th component's center, and θ_i is its rotation angle relative to the global Cartesian coordinate system. Parameters (u_0^i, v_0^i, θ_i) allow for rigid translation and rotation of the component. Next, the Cartesian coordinates are transformed into polar coordinates (r, φ)

Fig. 4 Schematic illustration of a local spline component with $nr = 8$



$$r = \sqrt{(u')^2 + (v')^2}, \quad (10)$$

$$\varphi = \arctan\left(\frac{v'}{u'}\right). \quad (11)$$

The boundary of the i -th spline-based component is then expressed in terms of a radial basis function as

$$\tilde{r}_i(\varphi) = \sum_{k=0}^{nr} R_{k,p}(\varphi) t_i^k, \quad (12)$$

where t_i^k represents the k -th shape control coefficient of the i -th component ($t_i^0 = t_i^k$ ensures a closed boundary), and $R_{k,p}(\varphi)$ is a NURBS radial basis function of degree p ($p = 2$ in this study). The NURBS radial basis function is defined as

$$R_{k,p}(\varphi) = \frac{N_{k,p}(\varphi) w_k}{\sum_{l=0}^{nr} N_{l,p}(\varphi) w_l}, \quad (13)$$

where w_k is the weight associated with the k -th basis function ($w_k = 1$ in this study), and $N_{k,p}$ is the k -th B-spline basis function defined using the Cox-De Boor recursive formula Eq. (3). Finally, the TDF $\phi_i(u, v)$ is expressed as

$$\phi_i(u, v) = 1 - \left(\frac{r}{\tilde{r}_i(\varphi) + eps} \right)^q, \quad (14)$$

where q is the shape index ($q = 2$ in this study) and $eps = 10^{-15}$ is a small value to prevent singularities. Benefits from the flexibility of NURBS-based modeling, complex local perturbation regions can be effectively represented. The design variable vector for the i -th spline-based component is expressed as $\mathbf{D}^i = (u_0^i, v_0^i, \theta_i, t_i^1, t_i^2, \dots, t_i^{nr}, h_i^*)$. The design variables of all local shape components are then assembled as $\mathbf{D}^l = (\mathbf{D}^1, \dots, \mathbf{D}^i, \dots, \mathbf{D}^{nc})$.

Up to this point, the global and local perturbations on the plane S have been defined separately. The global perturbation height field $h_S^g(\mathbf{x})$ is controlled by the design variable vector \mathbf{D}^g , while the local perturbation height field $h_S^l(\mathbf{x})$ is governed by \mathbf{D}^l , with \mathbf{D}^g and \mathbf{D}^l being independent of each other. The hierarchical perturbation expression for the plane S is given by

$$h_S^H(\mathbf{x}; \mathbf{D}) = h_S^g(\mathbf{x}; \mathbf{D}^g) + h_S^l(\mathbf{x}; \mathbf{D}^l), \quad (15)$$

where $\mathbf{D} = (\mathbf{D}^g, \mathbf{D}^l)$ represents the entire design variable vector. This process also indicates that global and local perturbations can be implemented concurrently.

2.3 Hierarchical shape variation for complex surfaces

In this subsection, we implement the hierarchical shape variation for a complex surface. For a given complex surface S , its hierarchical shape variation can be expressed as

$$\mathbf{x}^*(\mathbf{x}) = \mathbf{x} + h_S^H(\mathbf{x}; \mathbf{D}) \cdot \mathbf{N}(\mathbf{x}). \quad (16)$$

It should be noted that the perturbation height fields $h_S^g(\mathbf{x})$ and $h_S^l(\mathbf{x})$ discussed in the previous sections were defined within a planar rectangular domain. Hence, extending the definition to complex surfaces and constructing the hierarchical perturbation height field h_S^H represent a key challenge. To address this, the embedded perturbation height field approach is adopted. This method first maps the complex surface onto a standard parametric domain (rectangular). Within this domain, the global and local perturbation height fields $h_S^g(\mathbf{x})$ and $h_S^l(\mathbf{x})$ are defined. The hierarchical perturbation height field is then constructed and embedded back onto the complex surface.

Due to the surface complexity, parameterizing the complex surface onto the standard parametric domain remains a challenging task. With advancements in computational graphics, quasi-conformal and conformal mapping methods have been developed and widely applied in engineering (Choi et al. 2020; Guo et al. 2020). In this study, computational conformal mapping technique (Lui et al. 2013, 2014; Meng et al. 2016) are employed for surface parameterization.

Computational conformal mapping technique combines conformal mapping and surface parameterization to map the surface to a 2D parametric domain while minimizing angular distortion. The CCM technique has been applied to topology optimization (Huo et al. 2022), topography optimization (Huo et al. 2025), and stiffening optimization (Jiang et al. 2023) for shell structures. As shown in Fig. 5, this method employs a composite mapping consisting of two quasi-conformal maps with appropriate Beltrami coefficients to ensure conformality and bijectivity. The first quasi-conformal map uses a disk harmonic mapping, obtained by solving a partial differential equation. For a simply connected open surface S in the physical space, a harmonic mapping f_1 maps S to the unit disk $D(D \subset \mathbb{C})$ (Fig. 5a) and satisfies

$$\begin{cases} \Delta_S f_1 = 0, & \text{in } S, \\ f_1(\partial S) = \partial D, \end{cases} \quad (17)$$

where Δ_S is the Laplace–Beltrami operator defined on S . Equation (17) is solved using the finite element method (Pinkall and Polthier 1993). While f_1 achieves surface parameterization, it is generally not conformal. To address angular distortion, a second mapping f_2 is constructed using the quasi-conformal reconstruction method (Lui et al. 2014). Specifically, assuming $f_2(z = x + iy) = u(x, y) + iv(x, y) : D \rightarrow M$ is the second quasi-conformal mapping from D to the standard rectangular parameter domain M (Fig. 5b) and the Beltrami coefficient of the inverse map f_1^{-1} is $\mu_{h^{-1}} = \rho + i\tau$, then the quasi-conformal mapping f_2 can be solved through the following generalized Laplace equation

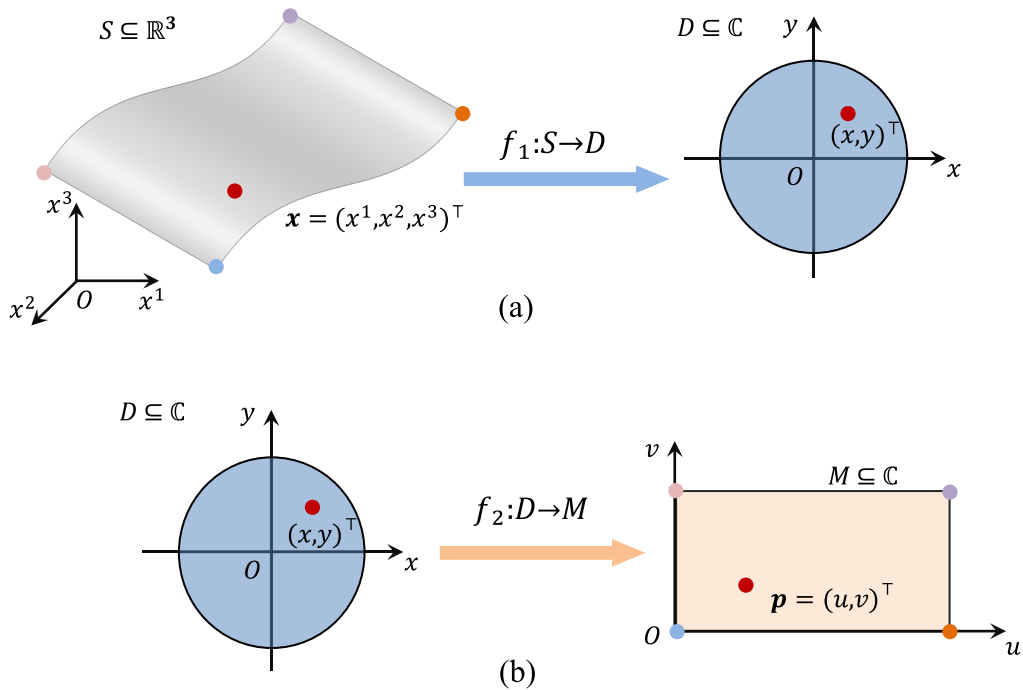


Fig. 5 Schematic illustration of solving the conformal mapping by composing two quasi-conformal mappings. **a** The first mapping. **b** The second mapping

$$\begin{cases} \nabla \cdot (\mathbf{A}(\nabla u)) = 0, & \text{in } D, \\ \nabla \cdot (\mathbf{A}(\nabla v)) = 0, & \text{in } D, \\ f_2(\partial D) = \partial M, \end{cases} \quad (18)$$

where $\nabla = \left(\frac{\partial}{\partial x}, \frac{\partial}{\partial y} \right)$, $\nabla(\cdot)$ is defined as the Euclidean gradient operator in the parametric domain, while $\nabla \cdot (\cdot)$ represents the corresponding divergence operator. $\mathbf{A} = \begin{pmatrix} \alpha_1 & \alpha_2 \\ \alpha_2 & \alpha_3 \end{pmatrix}$, with $\alpha_1 = \frac{(\rho-1)^2+\tau^2}{1-\rho^2-\tau^2}$, $\alpha_2 = -\frac{2\tau}{1-\rho^2-\tau^2}$, $\alpha_3 = \frac{(\rho+1)^2+\tau^2}{1-\rho^2-\tau^2}$. The composite conformal parameterization $f(S \rightarrow M)$ is then expressed as $f = f_2 \circ f_1$. Using computational conformal mapping technique, the surface S is mapped onto the parametric domain M . This enables the definition of the global and local perturbation height fields h_S^g and h_S^l and can be expressed as

$$h_S^g(\mathbf{x}; \mathbf{D}^g) = h_S^g(f^{-1}(\mathbf{p}); \mathbf{D}^g) = h_M^g(\mathbf{p}; \mathbf{D}^g), \quad (19)$$

$$h_S^l(\mathbf{x}; \mathbf{D}^l) = h_S^l(f^{-1}(\mathbf{p}); \mathbf{D}^l) = h_M^l(\mathbf{p}; \mathbf{D}^l), \quad (20)$$

where $h_M^g(\mathbf{p}; \mathbf{D}^g)$ and $h_M^l(\mathbf{p}; \mathbf{D}^l)$ are defined on M using the processes in Figs. 2 and 3, as described by Eqs. (2) and (8). Thus, the hierarchical perturbation height field on the surface can be expressed as

$$h_S^H(\mathbf{x}; \mathbf{D}) = h_M^g(\mathbf{p}; \mathbf{D}^g) + h_M^l(\mathbf{p}; \mathbf{D}^l). \quad (21)$$

Although the hierarchical perturbation height field h_S^H on the surface has been constructed through CCM technique, a prerequisite for this process is that the initial surface and the standard parametric domain must be homeomorphic. Considering that actual shell structures often exhibit more complex topological forms, the surface cutting operation and the multi-patch stitching scheme are further introduced to preprocess complex topological surfaces, thereby enhancing the applicability of the proposed method.

First, the surface cutting operation is described. For the cylindrical surface S to be designed, as shown in Fig. 6a, a cutting operation along the generatrix Γ is performed, yielding the intermediate surface \tilde{S} , which is topologically equivalent to a planar rectangle. The mapping f from \tilde{S} to its corresponding standard parametric domain M can then be obtained using computational conformal mapping technique (Fig. 6b, c). The global perturbation height field $h_{\tilde{S}}^g(\tilde{\mathbf{x}}; \mathbf{D}^g)$ and the local perturbation height field $h_{\tilde{S}}^l(\tilde{\mathbf{x}}; \mathbf{D}^l)$ on the intermediate surface \tilde{S} are constructed in accordance with Eqs. (19) and (20). It is worth noting that the cutting line Γ on the initial surface S splits into two curves, Γ_1 and Γ_2 , on the intermediate surface \tilde{S} . This split can result in inconsistencies in the height fields along Γ . To ensure continuity at the cutting line, the global and local perturbation height fields corresponding to Γ are processed as follows

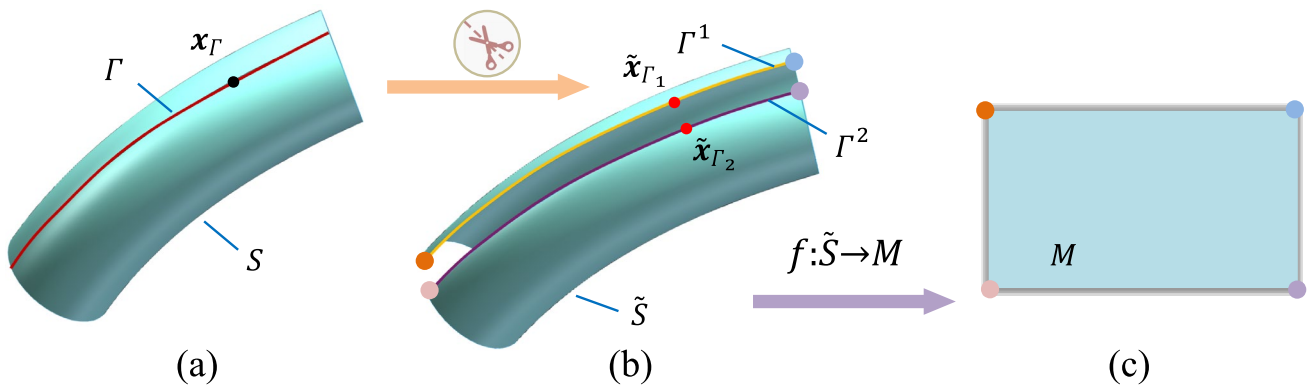


Fig. 6 The process of cylindrical shell computational conformal mapping based on the cutting operation

$$h_S^g(x; \mathbf{D}^g) = \begin{cases} h_{\tilde{S}}^g(\tilde{x}; \mathbf{D}^g), & \text{if } x \in S \setminus \Gamma, \\ \frac{1}{2} \cdot \left(h_{\tilde{S}}^g(\tilde{x}_{\Gamma_1}; \mathbf{D}^g) + h_{\tilde{S}}^g(\tilde{x}_{\Gamma_2}; \mathbf{D}^g) \right), & \text{if } x \in \Gamma. \end{cases} \quad (22)$$

$$h_S^l(x; \mathbf{D}^l) = \begin{cases} h_{\tilde{S}}^l(\tilde{x}; \mathbf{D}^l), & \text{if } x \in S \setminus \Gamma, \\ \max(h_{\tilde{S}}^l(\tilde{x}_{\Gamma_1}; \mathbf{D}^l), h_{\tilde{S}}^l(\tilde{x}_{\Gamma_2}; \mathbf{D}^l)), & \text{if } x \in \Gamma. \end{cases} \quad (23)$$

Through the surface cutting operation described above, the proposed method is capable of handling general complex surfaces. However, for highly intricate surfaces, such as the one illustrated in Fig. 7a, a direct mapping may result in numerical

instability. To address this issue, the multi-patch stitching scheme is introduced. The core concept of this approach is to decompose the initial complex surface into multiple simpler patches based on geometric features (Fig. 7b). The perturbation height fields are then defined separately on these simpler patches to achieve shape modifications (Fig. 7d). Finally, the patches are assembled (Fig. 7c) to form the complete analysis model. For the decomposed simpler patches, the definition of perturbation height fields requires further refinement. Let $S = \bigcup_{i=1}^{ns} S_i$ represent the intermediate surface composed of a set of patches, where S_i denotes the i -th patch, and ns is the total number of patches. The perturbation height field on each patch S_i can be defined following the procedures outlined earlier. Additionally, the perturbation height field $h_{S_i}^H$ on each

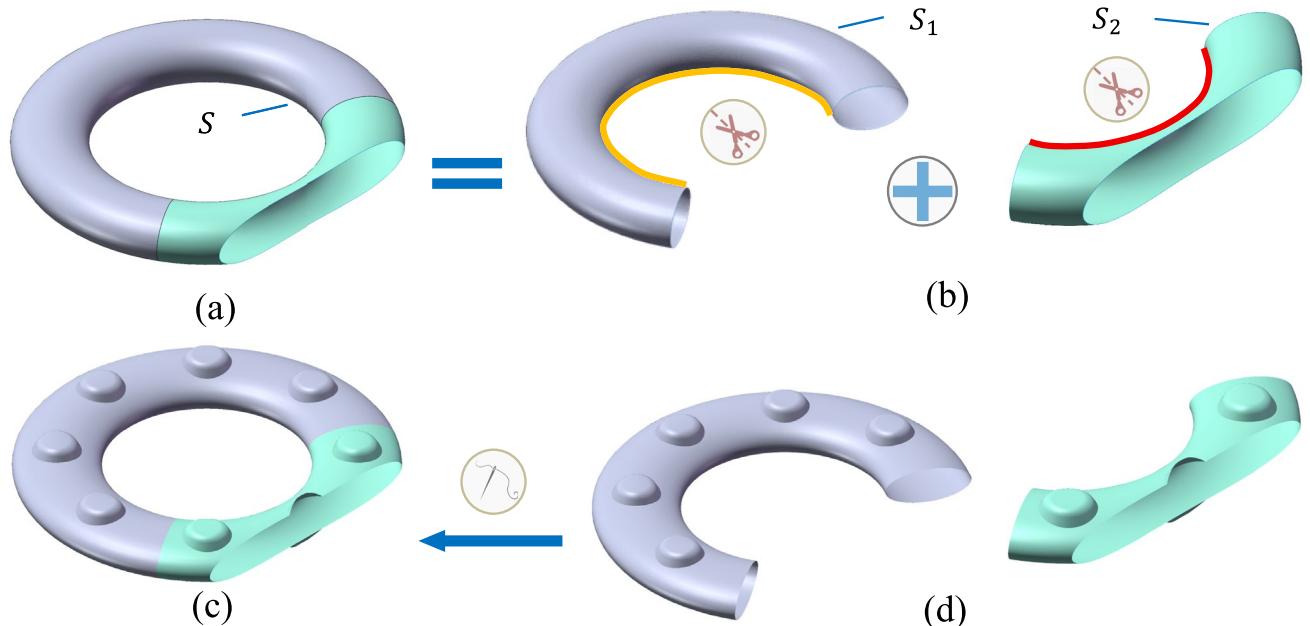


Fig. 7 The multi-patch stitching scheme. **a, b** The original surface is divided into two simple patches based on the geometry feature. **c** The hierarchical shape perturbation of the entire surface is obtained by

stitching together all the perturbed patches. **d** The shape perturbation of each patch is constructed via the approaches described earlier

patch can be extended to the entire intermediate surface S as follows

$$h_{S_i}^{s,H}(x;D^i) = \begin{cases} h_{S_i}^H(x;D^i), & \text{if } x \in S_i, \\ 0, & \text{if } x \notin S_i, \end{cases} \quad (24)$$

where D^i denotes the design variable vector corresponding to the i -th patch and the value 0 indicates that the perturbation is undefined outside the region S_i . The hierarchical shape perturbation height field h_S^H over the entire intermediate surface S is constructed through extension as

$$h_S^H = \max \left(h_{S_1}^{s,H}, h_{S_2}^{s,H}, \dots, h_{S_n}^{s,H} \right). \quad (25)$$

At the interfaces between surface patches, the height fields have been independently defined within each patch. Equation (25) ensures the coupling of the height fields across patch interfaces during the optimization process. Ultimately, by combining computational conformal mapping technique, the surface cutting operation, and the multi-patch stitching scheme, hierarchical shape variation for complex surfaces is achieved.

Furthermore, to ensure the differentiability of the function, the Kreisselmeier–Steinhauser (K–S) function (Kreisselmeier and Steinhauser 1980) is introduced to approximate the assembly operators in Eqs. (8), (23) and (25). This approximation is expressed as

$$\zeta = \max(\zeta^1, \dots, \zeta^n) \approx \frac{\ln(\sum_{i=1}^n \exp(l\zeta^i))}{l}, \quad (26)$$

where l is a large positive constant ($l = 100$ in this study). In addition, the Heaviside function we utilized in this study is expressed as

$$H_{\alpha,\epsilon}(x) = \begin{cases} 1, & \text{if } x > \epsilon, \\ \frac{3}{4} \left(\frac{x}{\epsilon} - \frac{x^3}{3\epsilon^3} \right) + \frac{1+\epsilon}{2}, & \text{if } |x| \leq \epsilon, \\ 0, & \text{otherwise,} \end{cases} \quad (27)$$

where $\epsilon = 0.6$ is the width of numerical approximation. To avoid the interrupt height variation at the point $x = 0$, the specific Heaviside function H^* is obtained by the horizontal movement, i.e. $H^*(x) = H_{\alpha,\epsilon}(x - \epsilon)$.

3 Optimization formulation and sensitivity analysis

3.1 Optimization formulation

In this study, a hierarchical shape optimization problem is formulated to minimize the compliance of shell structures. The material is assumed to be linearly elastic, isotropic, and

homogeneous. Let $S(D)$ denote the middle surface of the shell after hierarchical shape perturbation, with $S_0 = S(\mathbf{0})$ representing the initial middle surface. The perturbed shell structure occupies a volumetric domain defined as $\Omega(D, t) = S(D) \times [-\bar{t}/2, \bar{t}/2]$, where t is the thickness coordinate and \bar{t} is the shell thickness (as illustrated in Fig. 8a). Under the proposed framework, the hierarchical shape optimization problem is formulated as follows

$$\text{Find } D = (D^g, D^l), U(x;D) \quad (28a)$$

$$\text{Minimize } C = C(U(x;D), D) = \int_{\Omega(D,t)} (\mathbf{F}(D) \cdot \mathbf{U}(x;D)) dV \quad (28b)$$

s.t.

$$\begin{aligned} & \int_{\Omega(D,t)} (C^{\alpha\beta\lambda\mu} e_{\alpha\beta}(U(x;D)) e_{\lambda\mu}(V(x;D)) + D^{\alpha\lambda} e_{\alpha 3}(U(x;D)) e_{\lambda 3}(V(x;D))) dV \\ & = \int_{\Omega(D,t)} (\mathbf{F}(D) \cdot \mathbf{V}(x;D)) dV, \quad \forall V(x;D) \in U_{ad}, \end{aligned} \quad (28c)$$

$$U(x;D) \in U, D \in \mathcal{U}_D, \quad (28d)$$

where C represents the structural compliance, and \mathbf{F} denotes the external force applied to the structure. The tensors $C^{\alpha\beta\lambda\mu}$ and $D^{\alpha\lambda}$ correspond to the in-plane and out-of-plane constitutive tensors in the curvilinear coordinate system, respectively. The primary displacement $\mathbf{U}(x;D)$ belongs to the prescribed constraint set U , while the virtual displacement field $\mathbf{V}(x;D)$ belongs to the admissible set U_{ad} . These two displacements both satisfy the Reissner–Mindlin kinematical assumption. The terms $e_{\alpha\beta}(\cdot)$ and $e_{\alpha 3}(\cdot)$ denote the surface strain tensor (including membrane and bending behavior) and the transverse shear strain tensor, respectively (Chapelle and Bathe 2011). The set \mathcal{U}_D defines the feasible space for the design variable vector D . For thin shell models, the transverse shear effect is neglected and will not be discussed further.

3.2 Analytical sensitivity

In Eq. (28), the integration domain $\Omega(D, t)$ changes during the design process, making the proposed hierarchical shape optimization inherently a boundary evolution problem. Thus, the shape sensitivity analysis is required to compute the derivatives of the objective and constraint functions concerning the design variables (Choi and Kim 2004).

To simplify the explanation, let d denote an arbitrary element of the design variable vector D , which controls the shape of the shell structure. Suppose $I(W) = \int_{\Omega(d,t)} W dV$ is a general structural response (where $I(W)$ satisfies the regularity requirements of the design domain and some smoothness conditions), and $W = W(\mathbf{U}(x;d), \mathbf{V}(x;d))$ is a functional of $\mathbf{U}(x;d)$ and $\mathbf{V}(x;d)$. Here, $\mathbf{U}(x;d)$ and $\mathbf{V}(x;d)$ are

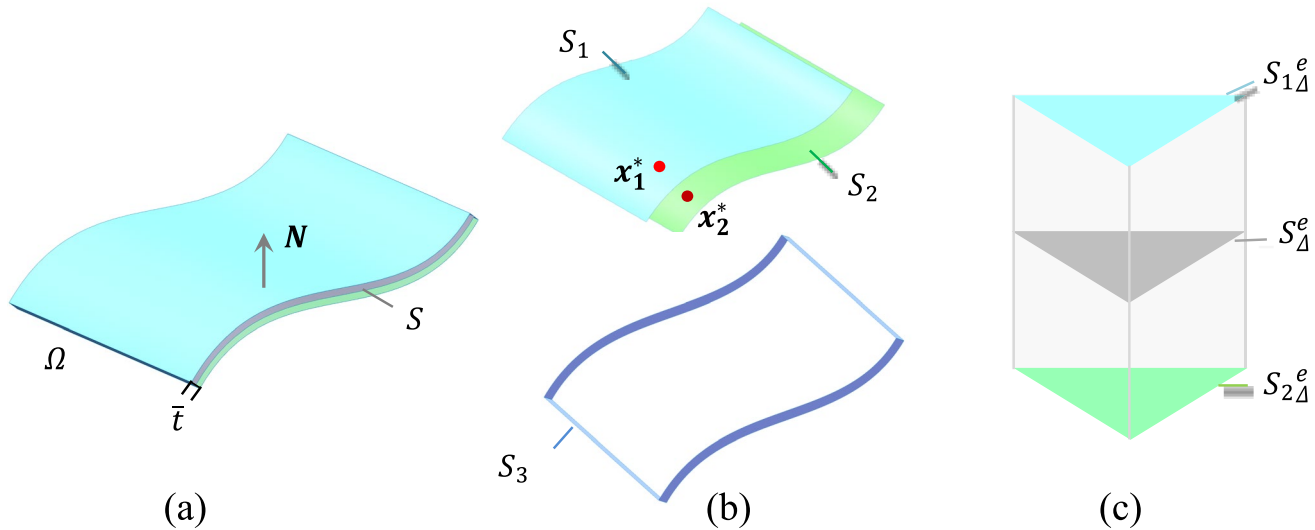


Fig. 8 **a** Schematic illustration of the relationship of the middle surface with the bulk domain. **b** The boundary of the bulk domain is decomposed into three parts. **c** Representation of the bulk domain in

the discrete level, where S_{Δ}^e , $S_{1\Delta}^e$, $S_{2\Delta}^e$ represent the intermediate surface S , the upper boundary surface S_1 , and the lower boundary surface S_2 of the discretized shell, respectively

displacements corresponding to $\mathbf{U}(\mathbf{x}; \mathbf{D})$ and $\mathbf{V}(\mathbf{x}; \mathbf{D})$, respectively. According to the Raynold's transport theorem (Fung 1977), the material derivative of $I(W)$ is

$$(I(W))^\circ = \int_{\Omega(d,t)} ((W)' + \operatorname{div}(Wv)) dV, \quad (29)$$

where the symbols $(\cdot)^\circ = \frac{D(\cdot)}{Dd}$ and $(\cdot)' = \frac{\partial(\cdot)}{\partial d}$ represent the material and spatial derivatives, respectively. $\operatorname{div}(\cdot)$ is the divergence operator, and the symbol v is the velocity field induced by an instant change of the parameter d . By leveraging the Gauss theorem, the second term in Eq. (29) is reduced to the boundary $\partial\Omega(d, t)$ as

$$\int_{\Omega(d,t)} \operatorname{div}(Wv) dV = \int_{\partial\Omega(d,t)} WV_n dS, \quad (30)$$

where $V_n = v \cdot N$ with N representing the outer normal vector defined on $\partial\Omega(d, t)$, and we have

$$(I(W))^\circ = \int_{\Omega(d,t)} (W)' + \int_{\partial\Omega(d,t)} WV_n dS. \quad (31)$$

With the material derivative defined as in the above expression, we now proceed to the sensitivity analysis. We denote the integrand of the left-hand side of Eq. (28c) as $W_C = W_C(\mathbf{U}(\mathbf{x}; d), \mathbf{V}(\mathbf{x}; d))$, which represents the generalized strain energy density. According to Chapelle and Bathe (2011), taking the spatial derivative of W_C , we have

$$(W_C)' = W_C(\mathbf{U}'(\mathbf{x}; d), \mathbf{V}(\mathbf{x}; d)) + W_C(\mathbf{U}(\mathbf{x}; d), \mathbf{V}'(\mathbf{x}; d)). \quad (32)$$

According to Eq. (31), the material derivative of the left-hand side of Eq. (28c) can be written as

$$(I(W_C))^\circ = \int_{\Omega(d,t)} (W_C(\mathbf{U}'(\mathbf{x}; d), \mathbf{V}(\mathbf{x}; d)) + W_C(\mathbf{U}(\mathbf{x}; d), \mathbf{V}'(\mathbf{x}; d))) dV + \int_{\partial\Omega(d,t)} W_C V_n dS. \quad (33)$$

Similarly, let $W_F(\mathbf{U}(\mathbf{x}; d), \mathbf{V}(\mathbf{x}; d))$ be the integrand of the right-hand side of Eq. (28c). Here, $W_F = \mathbf{F}(d) \cdot \mathbf{V}(\mathbf{x}; d)$. Then, the material derivative of the right-hand side of Eq. (28c) can be written as

$$(I(W_F))^\circ = \int_{\Omega(d,t)} (W_F)' dV + \int_{\partial\Omega(d,t)} W_F V_n dS. \quad (34)$$

Taking the spatial derivative of W_F , we have

$$(W_F)' = \mathbf{F}'(d) \cdot \mathbf{V}(\mathbf{x}; d) + \mathbf{F}(d) \cdot \mathbf{V}'(\mathbf{x}; d) = \mathbf{F}'(d) \cdot \mathbf{V}(\mathbf{x}; d) + W_F(\mathbf{U}(\mathbf{x}; d), \mathbf{V}'(\mathbf{x}; d)). \quad (35)$$

Furthermore, from Eq. (28c), we get

$$\begin{aligned} & \int_{\Omega(d,t)} W_C(\mathbf{U}(\mathbf{x}; d), \mathbf{V}'(\mathbf{x}; d)) dV \\ &= \int_{\Omega(d,t)} W_F(\mathbf{U}(\mathbf{x}; d), \mathbf{V}'(\mathbf{x}; d)) dV, \end{aligned} \quad (36)$$

and

$$(I(W_C))^\circ = (I(W_F))^\circ. \quad (37)$$

Combining Eqs. (33–37), we obtain

$$\begin{aligned} & \int_{\Omega(d,t)} W_C (\mathbf{U}'(\mathbf{x};d), \mathbf{V}(\mathbf{x};d)) dV + \int_{\partial\Omega(d,t)} W_C V_n dS \\ &= \int_{\Omega(d,t)} \mathbf{F}'(d) \cdot \mathbf{V}(\mathbf{x};d) dV + \int_{\partial\Omega(d,t)} W_F V_n dS. \end{aligned} \quad (38)$$

Since $\mathbf{U}(\mathbf{x};d) = \mathbf{V}(\mathbf{x};d)$ in the concerned compliance minimization problem (Guo et al. 2014), the compliance function satisfies

$$C = \int_{\Omega(d,t)} W_C (\mathbf{U}(\mathbf{x};d), \mathbf{U}(\mathbf{x};d)) dV. \quad (39)$$

Thus, by substituting Eqs. (33) and (38–39), the material derivative of the objective function C is derived as

$$(C)^\circ = 2 \int_{\Omega(d,t)} \mathbf{F}'(d) \cdot \mathbf{U}(\mathbf{x};d) dV + \int_{\partial\Omega(d,t)} (2W_F - W_C) V_n dS. \quad (40)$$

It can be observed that the term involving $\mathbf{U}'(\mathbf{x};d)$ has been eliminated in the final expression, thereby reducing the computational complexity and cost of solving the sensitivity. Since load-dependent design problems are not considered in this study, Eq. (40) can be further simplified as

$$(C)^\circ = \int_{\partial\Omega(d,t)} -W_C V_n dS. \quad (41)$$

3.3 Computation of the velocity field

Thus far, the sensitivity analysis remains incomplete, since it is still necessary to compute the geometric quantity V_n in Eq. (41), where $V_n = \mathbf{v} \cdot \mathbf{N}$. It is important to note that V_n is only evaluated on $\partial\Omega(d,t)$. Given that $\Omega(d,t) = S(d) \times [-\tilde{t}/2, \tilde{t}/2]$ (as shown in Fig. 8a), the boundary of the volume domain is expressed as

$$\partial\Omega(d,t) = \bigcup_{i=1}^3 S_i, \quad (42)$$

where $S_i (i = 1, 2, 3)$ represent the outer surfaces of the shell structure (as illustrated in Fig. 8b).

For any point $\mathbf{x}^* = \mathbf{x}^*(\mathbf{x};d)$ on the middle surface $S(d)$, its position is obtained by perturbing the corresponding point \mathbf{x} on the initial middle surface S_0 , such that

$$\mathbf{x}^*(\mathbf{x};d) = \mathbf{x} + h_S^H(\mathbf{x};d) \cdot \mathbf{N}(\mathbf{x}, S_0), \quad (43)$$

where $\mathbf{N}(\mathbf{x}, S_0)$ represents the unit normal at point \mathbf{x} on the initial surface S_0 .

Consequently, the positions of points \mathbf{x}_1^* on the upper boundary surface S_1 and \mathbf{x}_2^* on the lower boundary surface S_2 can be expressed as

$$\mathbf{x}_1^* = \mathbf{x}^* + \frac{\tilde{t}}{2} \mathbf{N}(\mathbf{x}^*, S(d)), \quad (44)$$

$$\mathbf{x}_2^* = \mathbf{x}^* - \frac{\tilde{t}}{2} \mathbf{N}(\mathbf{x}^*, S(d)), \quad (45)$$

where $\mathbf{N}(\mathbf{x}^*, S(d))$ is the normal vector at \mathbf{x}^* on the perturbed middle surface $S(d)$.

Next, the velocity field induced by an instant change of the design variable d is derived, using the upper boundary surface S_1 as an example. Substituting Eq. (43) into Eq. (44) gives

$$\mathbf{x}_1^*(\mathbf{x};d) = \mathbf{x} + h_S^H(\mathbf{x};d) \cdot \mathbf{N}(\mathbf{x}, S_0) + \frac{\tilde{t}}{2} \mathbf{N}(\mathbf{x}^*, S(d)). \quad (46)$$

The velocity field \mathbf{v}_1 of boundary S_1 is defined as the material derivative of \mathbf{x}_1^* with respect to d , yielding

$$\mathbf{v}_1 = (\mathbf{x}_1^*(\mathbf{x};d))^\circ = \frac{\partial h_S^H(\mathbf{x};d)}{\partial d} \cdot \mathbf{N}(\mathbf{x}, S_0) + \frac{\tilde{t}}{2} \frac{\partial \mathbf{N}(\mathbf{x}^*, S(d))}{\partial d}. \quad (47)$$

Similarly, the velocity field \mathbf{v}_2 of boundary S_2 is expressed as

$$\mathbf{v}_2 = (\mathbf{x}_2^*(\mathbf{x};d))^\circ = \frac{\partial h_S^H(\mathbf{x};d)}{\partial d} \cdot \mathbf{N}(\mathbf{x}, S_0) - \frac{\tilde{t}}{2} \frac{\partial \mathbf{N}(\mathbf{x}^*, S(d))}{\partial d}. \quad (48)$$

Since $V_n = \mathbf{v} \cdot \mathbf{N}$, it follows that

$$V_n^1 = \mathbf{v}_1 \cdot \mathbf{N}(\mathbf{x}_1^*, S_1), \quad (49)$$

$$V_n^2 = \mathbf{v}_2 \cdot \mathbf{N}(\mathbf{x}_2^*, S_2), \quad (50)$$

where $\mathbf{N}(\mathbf{x}_i^*, S_i)$ represents the normal vector at \mathbf{x}_i^* of boundary S_i and V_n^i represents the normal velocity field of boundary S_i . Given that the thickness of the shell structure is relatively small compared to its in-plane dimensions, the effect of boundary S_3 on Eq. (41) is neglected. Since $h_S^H(\mathbf{x};d)$ is defined using the surface cutting operation and multi-patch stitching scheme, its spatial derivative with respect to d can be expressed as

$$\frac{\partial h_S^H(\mathbf{x};d)}{\partial d} = \frac{\partial h_{S_i}^H}{\partial d} \frac{\partial h_{S_i}^{S,H}}{\partial h_{S_i}^H} \frac{\partial h_{S_i}^H}{\partial d}, \quad (51)$$

where $h_{S_i}^H$ is the hierarchical perturbation height field defined on the i -th patch S_i , and $h_{S_i}^{S,H}$ is expressed using Eq. (24). Here, \tilde{S}_i denotes the intermediate surface obtained from the surface cutting operation on S_i , and $h_{\tilde{S}_i}^H$ is obtained from the conformal mapping $f_i(\mathbf{x}) = \mathbf{p} : \tilde{S}_i \rightarrow M_i$ as $h_{\tilde{S}_i}^H(\mathbf{x};d) = h_{M_i}^H(\mathbf{p};d)$.

Benefiting from the perturbation pattern defined in Eq. (15), the partial derivative of $h_{M_i}^H(\mathbf{p};d)$ with respect to the overall design variable vector \mathbf{D} can be expressed as

$$\frac{\partial h_{M_i}^H(\mathbf{p};\mathbf{D}_i)}{\partial D_i} = \left[\frac{\partial h_{M_i}^g(\mathbf{x};D_i^g)}{\partial D_i^g}, \mathbf{0}^l \right] + \left[\mathbf{0}^g, \frac{\partial h_{M_i}^l(\mathbf{x};D_i^l)}{\partial D_i^l} \right], \quad (52)$$

where $h_{M_i}^H(\mathbf{p}; \mathbf{D}_i)$ and $\mathbf{D}_i = (\mathbf{D}_i^g, \mathbf{D}_i^l)$ represent the hierarchical perturbation height field and shape design variable vector on the i -th parameter domain, respectively.

4 Numerical implementation and design process

4.1 Discrete sensitivity calculation

In this study, the finite element analysis of the shell structure is carried out using S3 elements in the commercial software Abaqus, which are suitable for both thin and thick shell structures. The structural response (stress, strain, etc.) is then extracted to compute the objective function and numerical sensitivities. In addition, we set five integration points along the thickness direction of the shell elements and adopt Simpson's rule for numerical integration.

To calculate Eq. (41) numerically, the perturbed surface $S(d)$ is discretized into a triangular mesh, denoted as

$$S_\Delta(d) = \bigcup_{e=1}^{n_e} S_\Delta^e(d), \quad (53)$$

where $S_\Delta^e(d)$ represents the e -th shell element (Fig. 8c). The discretized volume domain is defined as

$$\Omega_\Delta(d, t) = \bigcup_{e=1}^{n_e} \Omega_\Delta^e(d, t) = \bigcup_{e=1}^{n_e} S_\Delta^e(d) \times \left[-\frac{\tilde{t}}{2}, \frac{\tilde{t}}{2}\right], \quad (54)$$

where $\Omega_\Delta(d, t)$ represents the volume occupied by the e -th shell element. Thus, the discrete form of Eq. (40) is expressed as

$$(C)^\circ = \sum_{e=1}^{n_e} \left((-W_C V_n^1)_e^1 + (-W_C V_n^2)_e^2 \right) A_e, \quad (55)$$

where A_e represents the area of S_Δ^e , and $(\cdot)_e^1, (\cdot)_e^2$ correspond to the values of the quantity (\cdot) at $S_{1\Delta}^e$ and $S_{2\Delta}^e$, respectively.

4.2 Design process

In this subsection, we briefly summarize the overall hierarchical shape optimization workflow, as illustrated in Fig. 9. First, the unstructured triangular mesh is generated on the middle surface of the initial shell model (Fig. 9a). For complex shell structures, the surface mesh can be partitioned into multiple regions based on geometric features (Fig. 7), and simpler middle surfaces can be obtained through the surface cutting operation (Fig. 6). The middle surface is then parameterized using the CCM technique, and a hierarchical perturbation height field is defined within the parametric domain (Fig. 9b). This defined height field is subsequently applied to the initial mesh in Fig. 9a to generate the perturbed surface geometry (Fig. 9c). Finally, finite element analysis and sensitivity analysis are performed, and the design variables are updated iteratively until convergence is achieved by repeating the process shown in Fig. 9b–d.

5 Numerical examples

In this section, numerical examples are presented to validate the effectiveness of the proposed algorithm. Key factors that may influence the final design are also analyzed in detail. Unless otherwise specified, all geometric dimensions and material properties are treated as dimensionless parameters.

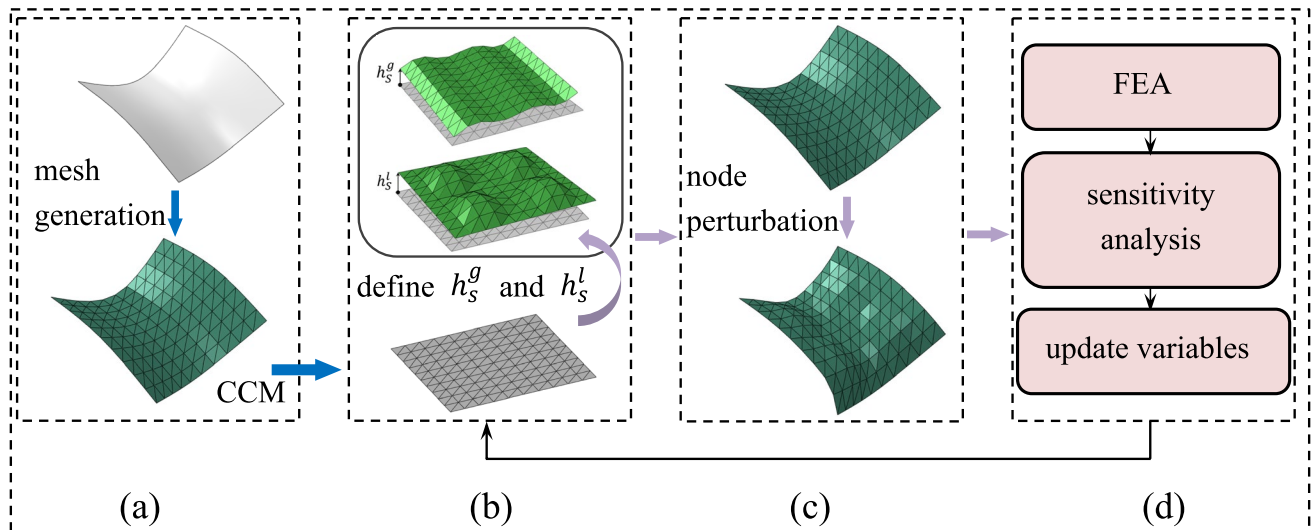


Fig. 9 Schematic diagram of the design process

The material is assumed to be isotropic and linearly elastic, with Young's modulus $E = 1$ and Poisson's ratio $\nu = 0.3$. The objective of the optimization problem is to minimize structural compliance (Eq. (28b)). The Method of Moving Asymptotes (MMA) (Svanberg 1987) is employed as the optimization solver to update the design variables. The proposed hierarchical shape optimization algorithm involves two types of design variables, D^g and D^l . The initial settings for each type of design variable are provided within the respective numerical examples. The optimization process is terminated at the 300th iteration.

5.1 Hierarchical shape optimization of a plate

To eliminate the influence of the mapping process and the curved geometry of shell structures, a simple square plate model is selected as a baseline example. This allows for a clear and intuitive demonstration of the effectiveness of the proposed hierarchical shape optimization method. The geometric model is illustrated in Fig. 10, with the plate thickness specified as 0.2. The primary design parameters are as follows: the global shape is governed by a 6×6 NURBS network, where the upper and lower bounds of the perturbation coefficients at the NURBS control points set to $h_{\max}^g = 10$ and $h_{\min}^g = 0$, respectively. The perturbation coefficients associated with the structural boundary are fixed at zero to preserve the boundary shape, while the initial values of the remaining coefficients are set to $\bar{h}^g = \frac{h_{\max}^g + h_{\min}^g}{2}$. The local shape is controlled by a 4×4 spline component layout, with the initial and maximum heights of each component set to $h_i^* = 1$ and $h_i^{*,\max} = 1$, respectively.

Based on the global design parameters, global-level shape optimization is first conducted. Since the mapping step is omitted, the global perturbation height field can be directly defined according to Eq. (2), and global shape variations are realized via Eq. (1). Figure 11 presents the iteration history and intermediate results of the global shape optimization. The objective function decreases rapidly and converges efficiently. From the overall structural shape, although the geometry is modified through normal perturbations at mesh nodes, a smooth shape is achieved without the need for additional filtering operations. Next, local shape design is performed using the local design parameters. As described in Sect. 2.2, the local perturbation height field can also be directly constructed. The entire process is depicted in Fig. 12. Local components move and merge quickly, ultimately forming rich morphological features on the plate surface, which significantly enhance structural performance. The final structure also exhibits a comparatively smooth geometric configuration.

Comparing the results in Figs. 11 and 12, it is evident that global and local shape optimization address shape

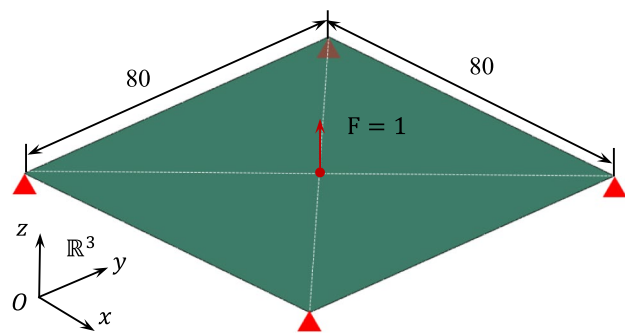


Fig. 10 Geometric schematic of the plate structure. The boundary conditions involve four fixed points, with a concentrated force applied at the center in the z -direction

design from different perspectives: the former focuses on the overall structural contour, while the latter emphasizes the refinement of detail. Although both approaches effectively improve structural performance, differences in the definitions of design variables and the scales of perturbations render direct or meaningful comparison inappropriate.

To achieve global shape control and local geometric refinement simultaneously, we implement the proposed hierarchical shape optimization method, performing concurrent optimization at both levels. The hierarchical optimization process is illustrated in Fig. 13, which demonstrates how the proposed method modifies the global shape while simultaneously capturing local details through spline components. The optimization history indicates that the objective function decreases rapidly and subsequently stabilizes, with the compliance function reduced from 250,767.60 to 467.98, representing a 99.81% decrease. This means a 536-fold improvement in structural stiffness. Compared to global or local optimization alone, the objective value is further reduced. The results in Fig. 14 provide an intuitive visualization of the optimized plate. Figure 14a–d shows that the hierarchical shape optimization method notably expands the design space, enriches the final design by integrating global and local modifications, and maintains structural smoothness. Figure 14e–h reveals that the substantial improvement in stiffness is primarily attributed to the wavy corrugations in the cross-section, which serve as a key feature of the optimized design. Additionally, local protrusions near the four fixed boundaries are found to effectively alleviate out-of-plane deformation induced by support reactions.

In summary, global-level, local-level, and hierarchical shape optimizations are applied to the plate model. Compared to single-level optimization approaches, the proposed hierarchical strategy not only improves overall structural performance but also enables detailed geometric refinement in local regions, demonstrating stronger synergistic optimization capability and greater design flexibility.

Fig. 11 Iteration histories and intermediate results of the global shape optimization of the plate structure, with $C_0 = 26568.09$, $C_{10} = 3053.26$, $C_{100} = 906.99$, $C_{200} = 905.75$, $C_{300} = 905.75$ (C_n represents the objective function value at the n th iteration step)

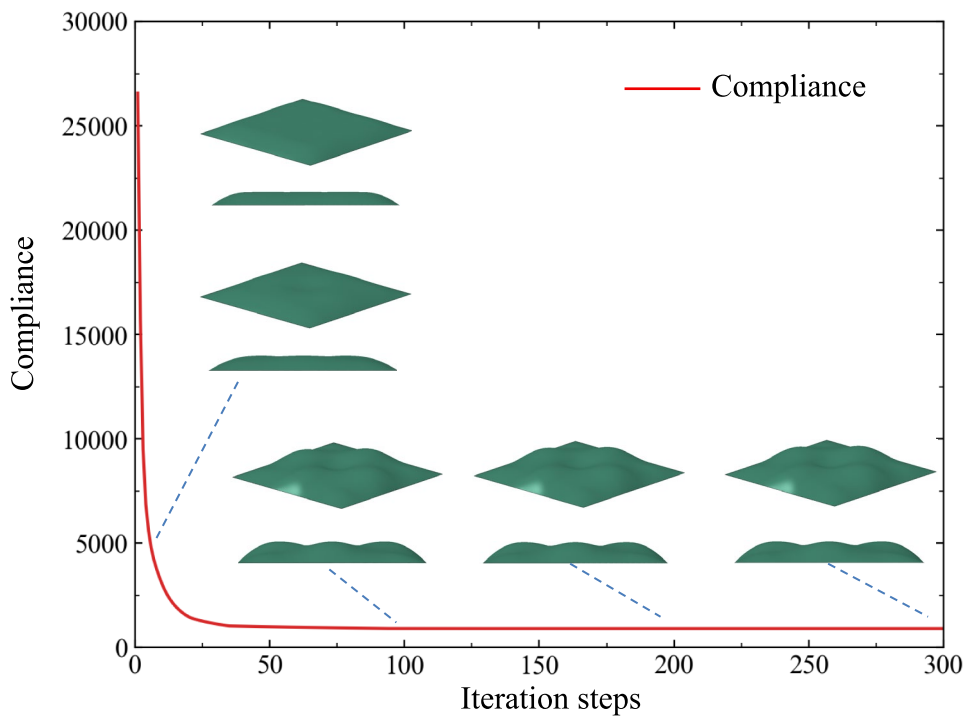
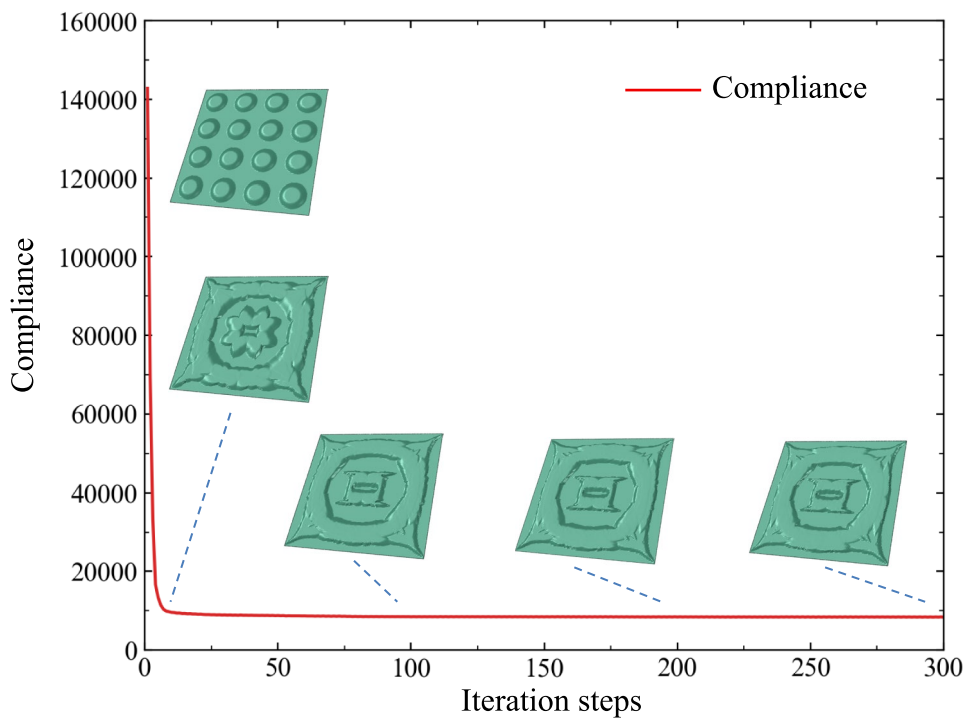


Fig. 12 Iteration histories and intermediate results of the local shape optimization of the plate structure, with $C_0 = 142787.61$, $C_{10} = 9609.59$, $C_{100} = 8496.65$, $C_{200} = 8443.92$, $C_{300} = 8409.01$



5.2 Hierarchical shape optimization of complex shells using CCM technique

In this subsection, several surface examples are presented to evaluate the effectiveness of the proposed algorithm in optimizing complex shell structures.

5.2.1 Conical shell structure

In this example, a conical shell reconstructed from a 3D point cloud (obtained via 3D scanning technology) is used to investigate the impact of different optimization strategies on the final design. The results indicate that, compared

Fig. 13 Iteration histories and intermediate results of the hierarchical shape optimization of the plate structure, with $C_0 = 15671.72$, $C_{10} = 1437.62$, $C_{100} = 686.96$, $C_{200} = 497.24$, $C_{300} = 467.98$

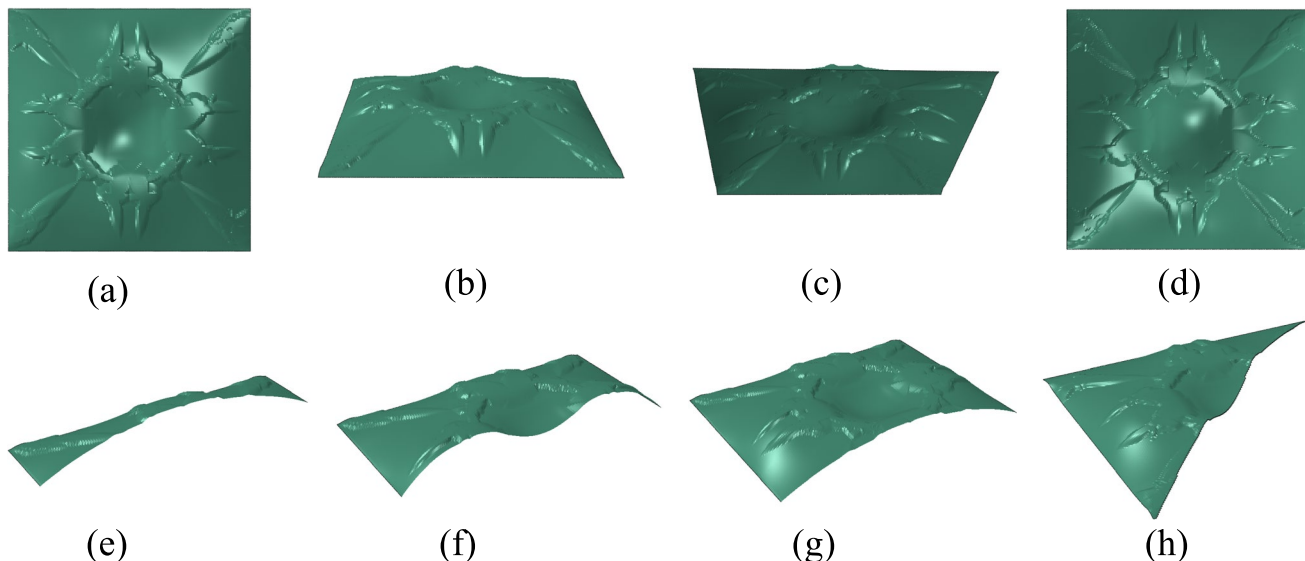
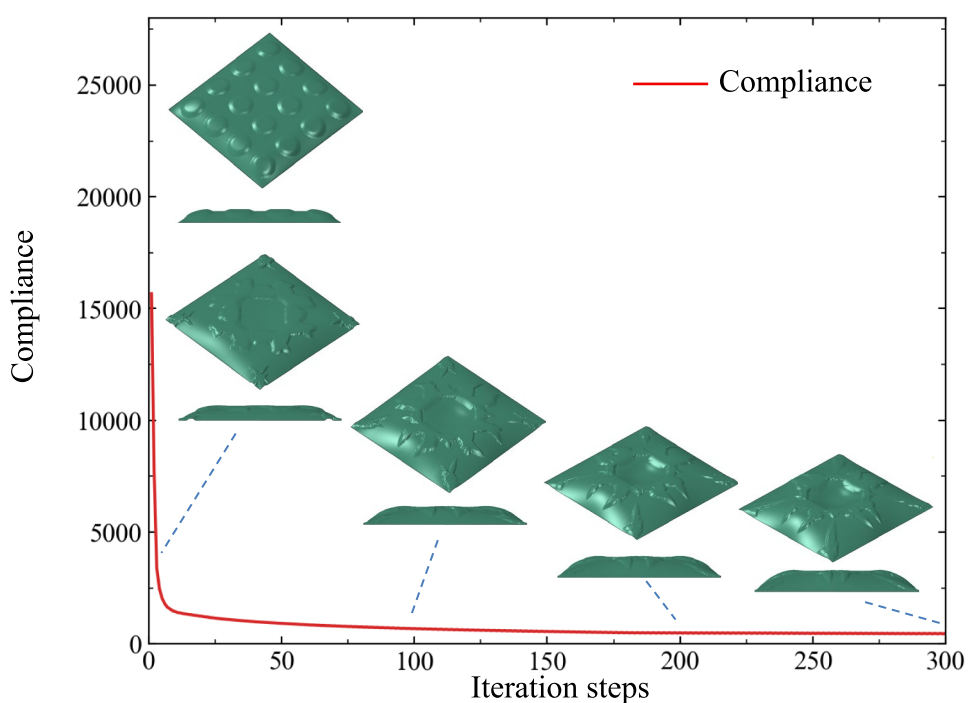


Fig. 14 Different views of the final design. **a** Front view 1. **b** Front view 2. **c** Back view 1. **d** Back view 2. **e** Cross-section at the transverse quarter position. **f** Cross-section at the transverse half position.

g Cross-section at the transverse three-quarters position. **h** Cross-section along the diagonal position

to sequential optimization—where global and local shape optimizations are conducted independently in a consecutive manner—the proposed hierarchical shape optimization (concurrent approach) achieves a lower objective function value and more reasonable design. The geometric dimensions

and boundary conditions of the conical shell are shown in Fig. 15. The primary design parameters for conical shell are as follows: the global shape is controlled by a 10×10 NURBS network, where the upper and lower bounds of the perturbation coefficients at the NURBS control points are set to $h_{\max}^g = 20$ and $h_{\min}^g = 0$, respectively. Similarly, the structural boundary shape is kept fixed, while the initial values of the remaining perturbation coefficients are set

to $\bar{h}^g = \frac{h_{\max}^g + h_{\min}^g}{2}$. The local shape is controlled by a 4×4 spline component layout, with the initial height and maximum height of each component set to $h_i^* = 4$ and $h_i^{*,\max} = 4$, respectively.

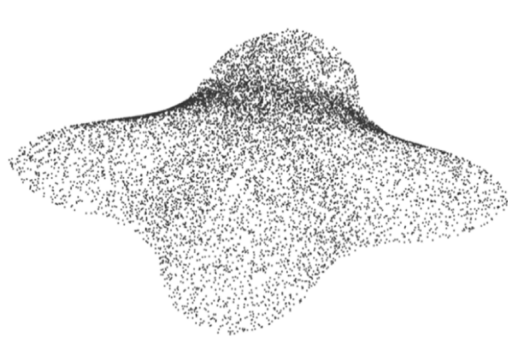
Initially, the middle surface of the shell is mapped onto the parametric domain using the CCM technique, where a hierarchical perturbation height field is defined to facilitate the hierarchical shape optimization design with the iteration history and intermediate results depicted in Fig. 16. The optimization process converges rapidly, producing a stable structural design. The final design in Fig. 16 reveals that local shape components are primarily concentrated around the loading points, enhancing local stiffness. For comparison, a sequential optimization strategy is employed. First, a global shape optimization is performed on the conical shell, and its iteration history is shown on the left side of Fig. 17. Through global shape modifications, a substantial increase in stiffness is observed. Subsequently, local shape optimization is applied after global shape optimization, as shown on the right side of Fig. 17. Although the optimization process converges quickly, its contribution to stiffness improvement is minimal. Additionally, the final design exhibits discontinuous local protrusions, which may compromise the overall load transfer efficiency. It is also worth noting that in this example, the global shape optimization shown on the left side of Fig. 17 converges relatively slowly, in sharp contrast to the rapid convergence observed in the global optimization of the plate model in Fig. 11. This difference in convergence behavior may be attributed to the influence of the initial configuration on the exploration of the global shape design space. For global shape

optimization, improvements in structural performance often rely on large-scale geometric changes. However, the current example may already possess a relatively beneficial initial configuration, which could result in slower convergence during the early stage of iteration. In contrast, the hierarchical shape optimization strategy introduces fine-tuned local shape adjustments along with global shape variations, which may facilitate better exploration of the global design space. In regions with concentrated loadings, the presence of local geometric features can effectively enhance local stiffness, leading to the rapid convergence behavior observed in Fig. 16.

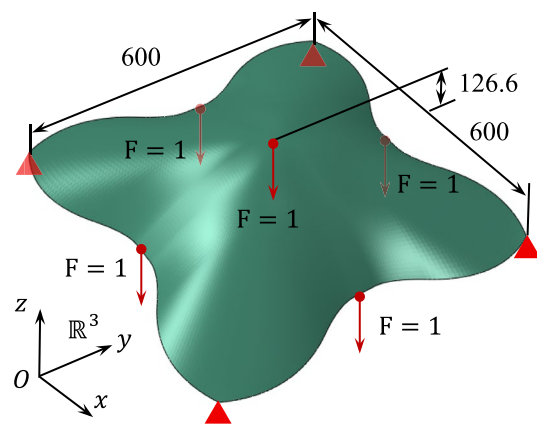
In summary, by comparing the results in Fig. 16 (300 iterations) and Fig. 17 (600 iterations), the proposed hierarchical shape optimization algorithm demonstrates both improved efficiency and superior design quality, further highlighting its effectiveness and computational advantage.

5.2.2 U-shaped shell structure

To verify the effectiveness and generality of the proposed hierarchical shape optimization method under complex geometric conditions, a shell structure with a complicated boundary contour is introduced, as shown in Fig. 18. Meanwhile, to explore the influence of global shape variations on structural performance, three NURBS networks with varying resolutions are employed to control the number of global shape design variables. The primary design parameters for this example are as follows: the global shape is controlled by 6×6 , 8×8 and 12×12 NURBS network, respectively. The upper and lower bounds of the perturbation coefficients at the NURBS control points are set to $h_{\max}^g = 20$ and $h_{\min}^g = 0$, respectively. Similarly, the structural boundary shape is kept



(a) The 3D point cloud



(b) Boundary conditions

Fig. 15 Problem settings of the conical shell example. The geometry model is reconstructed from the 3D point cloud data (a). b The shell structure (the thickness is set as 3) is fixed at four corners and sub-

jected to five concentrated forces (four at the middle of edges and one at the center of the surface). The forces are applied along the $-z$ direction

Fig. 16 Iteration histories and intermediate results of the hierarchical shape optimization of the conical shell structure, with $C_0 = 745.51$, $C_{10} = 185.38$, $C_{100} = 143.15$, $C_{200} = 140.33$, $C_{300} = 138.69$

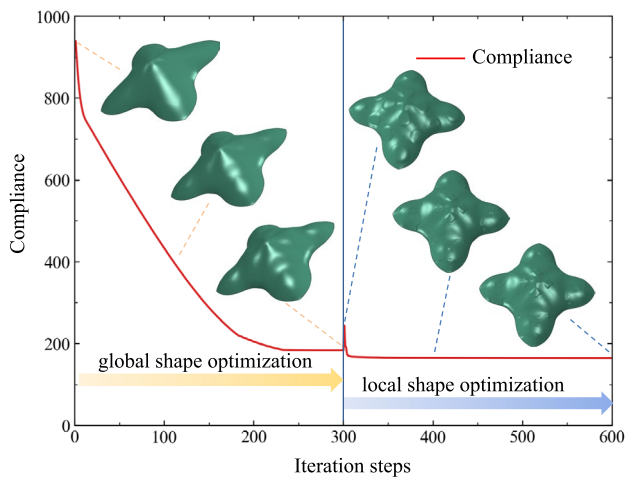
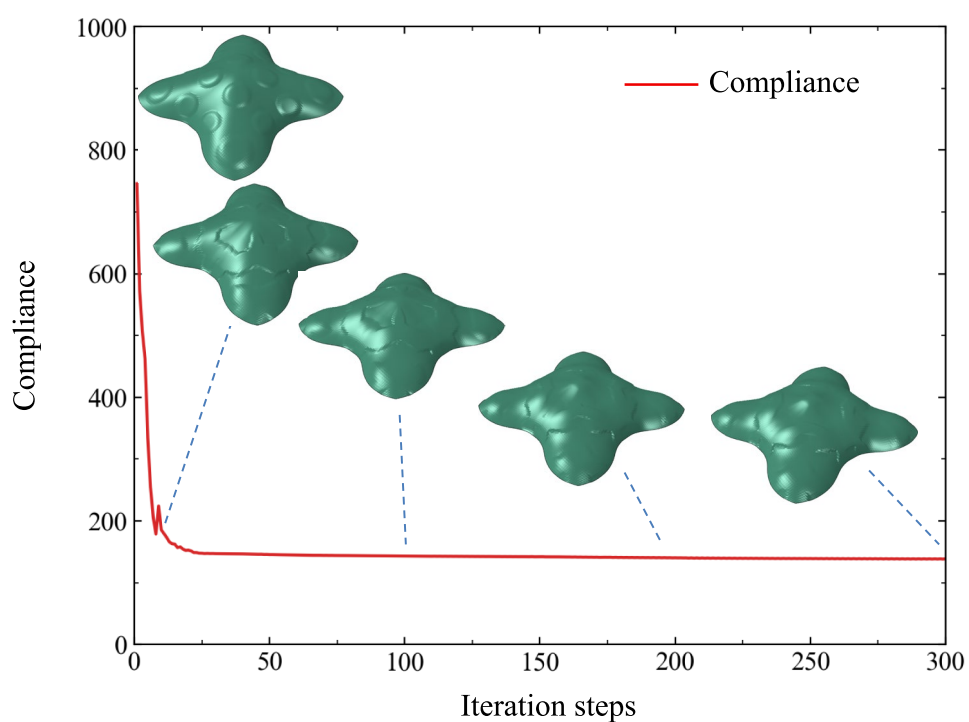


Fig. 17 Iteration histories and intermediate results of the sequential shape design for the conical shell structure. Before the 300th step, the iteration process utilizes the global shape design approach to optimize the structural performance, in which the compliance function is reduced from 938.92 to 184.06. At the 301st step, local shape optimization was performed, and the compliance function is ulteriorly reduced to 164.32

fixed, while the initial values of the remaining perturbation coefficients are set to $\bar{h}^g = \frac{h_{\max}^g + h_{\min}^g}{2}$. The local shape is controlled by a 4×6 spline component layout, with the initial height and maximum height of each component set to $h_i^* = 2$ and $h_i^{*,\max} = 2$, respectively.

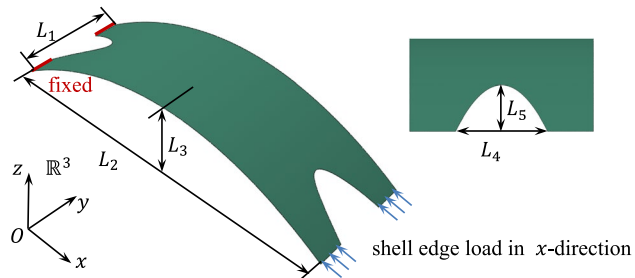


Fig. 18 Schematic geometric illustration of the U-shaped boundary shell structure. The geometric dimensions of the structure are $L_1 = 200\text{mm}$, $L_2 = 600\text{mm}$, $L_3 = L_4 = 100\text{mm}$, $L_5 = 50\text{mm}$, and thickness $t = 1\text{mm}$. In this example, the elastic modulus of the structure is $E = 70\text{Gpa}$ and the Poisson's ratio is $\nu = 0.3$. The boundary conditions consist of a fully fixed left edge and a shell edge load of 1N/mm applied along the x -direction at the right edge. Currently, the structural compliance is 26,868.56

Figure 19a–c shows the initial designs under three different parameter settings. Since the boundary shape is fixed while the interior region is assigned the initial perturbation coefficient \bar{h}^g , and each design employs a different number of global shape design variables. This results in the generation of distinct initial configurations, which exhibit different initial compliance values. Figure 19d–f further presents the corresponding final optimized results for each setting. It can be observed that as the global design resolution increases, the optimized geometries exhibit more pronounced and complex shape features. A distinct trend can

be observed, wherein more pronounced wavy undulations emerge in the structure, thereby enhancing its bending stiffness and reducing the objective function value. However, upon further comparison of the final objective values for the three cases, it becomes evident that the rate of improvement diminishes as the NURBS resolution increases. This observation might suggest that with further expansion of the NURBS network, the enhancement in structural stiffness tends to reach a state of convergence. In such cases, it becomes necessary to reasonably select parameter settings to balance structural performance and computational cost. Moreover, in practical engineering design, the design space is often constrained by factors such as manufacturing limitations and cost control. While high-resolution designs can offer better performance, they may also result in greater geometric complexity and increased manufacturing cost. Therefore, comparing the results under varying parameter settings offers meaningful differences, enabling designers to make more targeted trade-offs among performance, cost, and manufacturability, and providing greater flexibility for addressing diverse engineering demands.

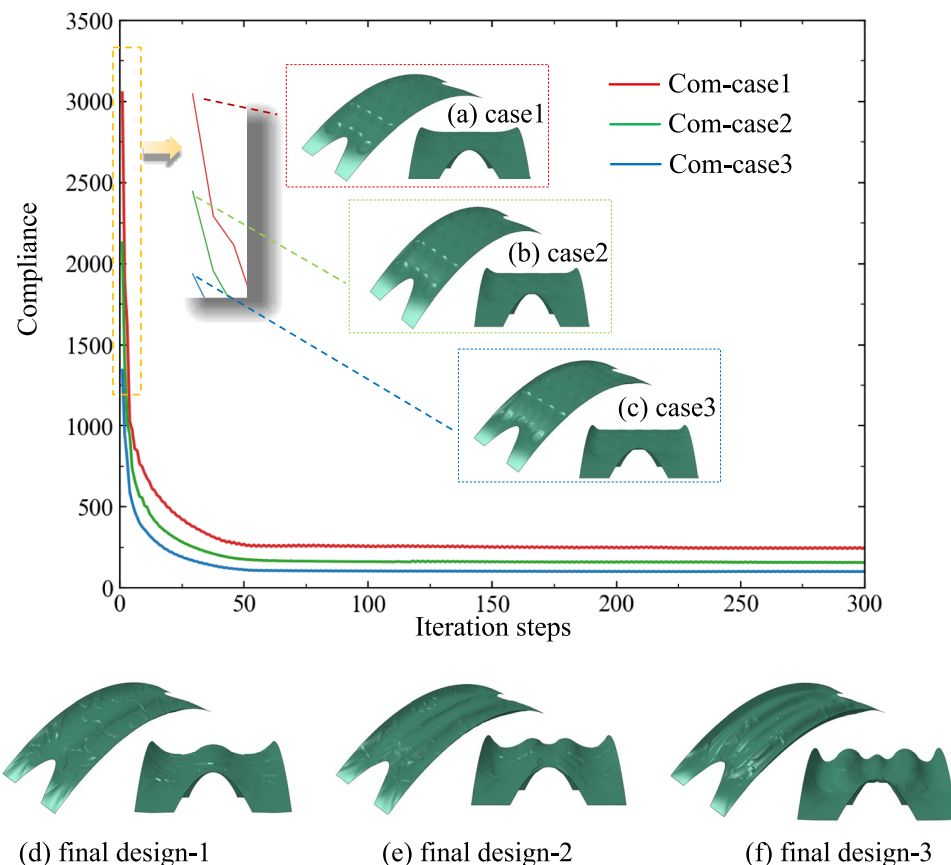
It should be noted that, based on mechanical intuition, the optimal structure in this example is expected to approach a flat plate. However, the reason the final structure remains curved arises from a feature of our shape optimization

approach, which is based on perturbations along the normal direction. Therefore, under the current optimization framework, the geometric transformation is restricted and the structure unable to fully degenerate into a flat plate.

5.2.3 Nozzle-shaped cylindrical shell structure

This example demonstrates the application of the surface cutting operation within the hierarchical shape optimization framework. The selected geometry is similar to the nozzle section of an engine exhaust system, with its geometric dimensions and boundary conditions shown in Fig. 20. The primary design parameters for this example are as follows: the global shape is controlled by 8×8 NURBS network, where the upper and lower bounds of the perturbation coefficients at the NURBS control points are set to $h_{\max}^g = 8$ and $h_{\min}^g = 0$, respectively. Unlike the previous cases, in this example, only the shape at the fixed end on the left side is constrained to remain unchanged, i.e., the perturbation coefficients in this region are fixed at zero throughout the optimization, while the initial values of the remaining perturbation coefficients are set to $\bar{h}^g = \frac{h_{\max}^g + h_{\min}^g}{2}$. The local shape is controlled by a 6×6 spline component layout, with

Fig. 19 Initial designs, iteration curves, and final designs obtained with different NURBS networks. **a–c** Initial designs corresponding to the cases of global shape network set as 6×6 , 8×8 and 12×12 , respectively. The compliance functions of the initial designs are 3054.82, 2128.34 and 1344.22, respectively. **d–f** The compliance functions of the final designs are 251.14, 158.69 and 100.21, respectively



the initial height and maximum height of each component set to $h_i^* = 1$ and $h_i^{*,\max} = 1$, respectively.

To enable parametric mapping, the surface cutting operation is applied, as illustrated by the cutting lines in Fig. 21a. This approach facilitates the construction of the initial hierarchical shape optimization design, depicted in Fig. 21b. The iteration history and intermediate results are shown in Fig. 22. During the first five iterations, the local shape components generated in the initial design quickly vanish, as seen in Fig. 22a–d. In subsequent iterations, shape modifications occur exclusively at the global level. From a mechanical perspective, for a cylindrical shell subjected to torsion, increasing the cross-sectional radius is an effective strategy for enhancing torsional stiffness, provided that thickness and material properties remain unchanged. Figure 22e, f demonstrates that the shell cross-section expands as much as possible, optimizing torsional rigidity. Moreover, the gradually transitioning toroidal surface near the fixed boundary helps to effectively reduce stress concentration. While previous examples highlight the advantages of hierarchical shape optimization in improving structural performance, this example reveals that under certain boundary conditions, the optimal configuration may be a completely smooth structure. During optimization, the algorithm rapidly eliminates local shape components to achieve a smooth configuration. This observation further validates the adaptability and effectiveness of the hierarchical shape optimization method,

demonstrating its capability to accommodate various structural design requirements.

5.2.4 Tee-branch pipe shell structure

In this final example, the multi-patch stitching scheme is utilized. The Tee-branch pipe shell structure, shown in Fig. 23a, cannot be directly mapped onto a planar domain due to its geometric complexity. To address this, the structure is decomposed into simpler surface patches (as illustrated in Fig. 23b), allowing for individual parameterization of each surface. This enables the implementation of hierarchical shape optimization through the multi-patch stitching scheme, as referenced in Fig. 7. In this example, identical design parameters are applied to each patch, with the main design parameters being: the global shape is controlled by 6×6 NURBS network, where the upper and lower bounds of the perturbation coefficients at the NURBS control points are set to $h_{\max}^g = 1$ and $h_{\min}^g = 0$, respectively. Only the shape at each pipe junction is fixed, i.e., the perturbation coefficients in this region are fixed at zero, while the initial values of the remaining perturbation coefficients are set to $\bar{h}^g = \frac{h_{\max}^g + h_{\min}^g}{2}$. The local shape is controlled by a 4×4 spline component layout, with the initial height and maximum height of each component set to $h_i^* = 0.1$ and $h_i^{*,\max} = 0.1$, respectively.

The initial design is depicted in Fig. 24a, while the iteration history and intermediate optimization results are shown in Fig. 24. The results indicate that compliance rapidly decreases and stabilizes at a converged value. The final optimized design reveals that distinct and complex shape modifications emerge throughout the structure due to the varying boundary conditions applied to each pipe section. For cylindrical pipe section II (Fig. 23b), its structural characteristics and boundary conditions closely resemble those in Sect. 5.2.3. Consequently, the optimized design eliminates local shape modifications, resulting in a smooth configuration. In contrast, for the non-circular pipe sections I and III, localized shape details develop around the pipes as the global shape undergoes minor adjustments. These

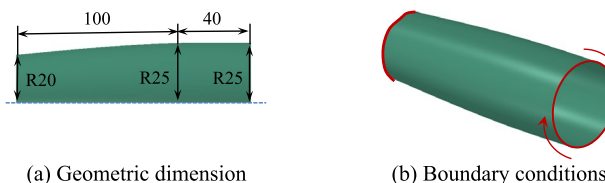


Fig. 20 Schematic illustration of the nozzle-shaped cylindrical shell structure. In this example, the shell thickness is set to 0.4, with boundary conditions consisting of a fixed constraint at the left end and a bending moment of 300 applied at the right end. The structural compliance without any design modifications is 1029.04

Fig. 21 The cutting line diagram of the nozzle-shaped cylindrical shell structure (the cutting operation referring to Fig. 6) and the initial design of the hierarchical shape optimization. The compliance corresponding to the initial design is 962.24

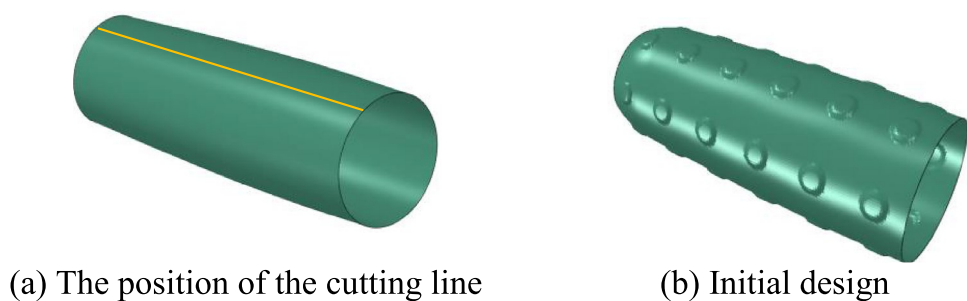


Fig. 22 Iteration histories and intermediate results of the hierarchical shape optimization of the nozzle-shaped cylindrical shell structure. (a)–(h) Represent the intermediate results at the 1st, 2nd, 3rd, 5th, 10th, 50th, 100th, and 300th iteration steps, respectively. The compliance at the 300th step is 471.18

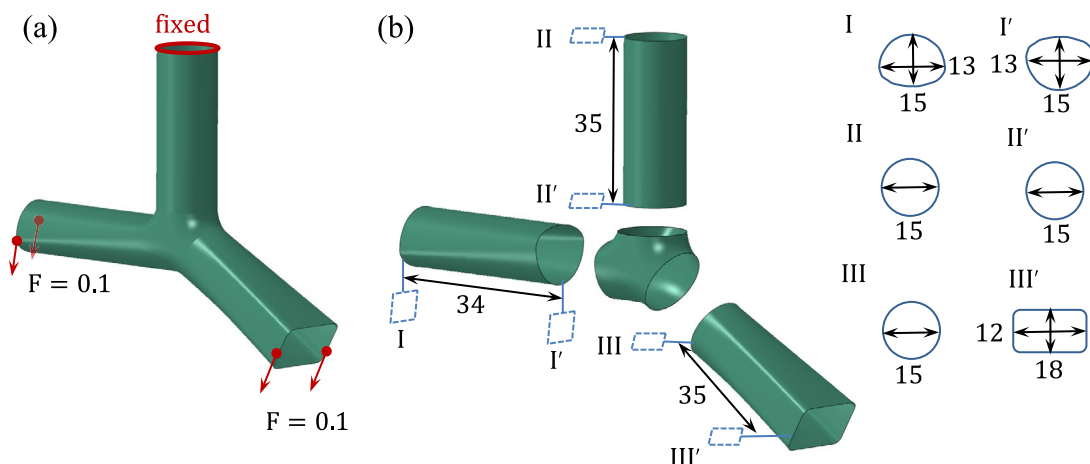
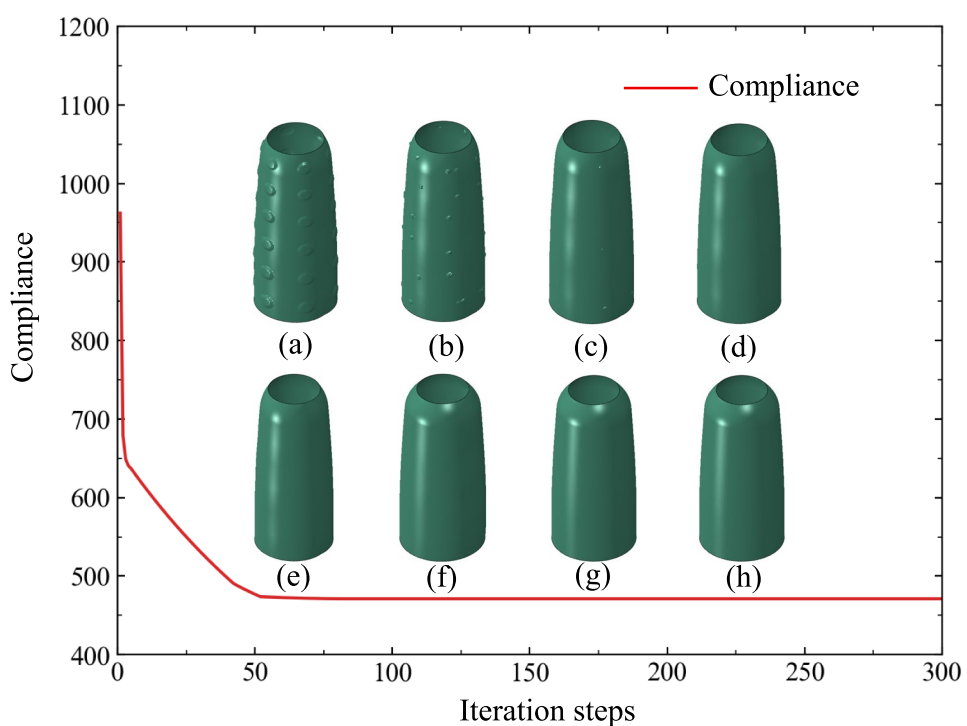


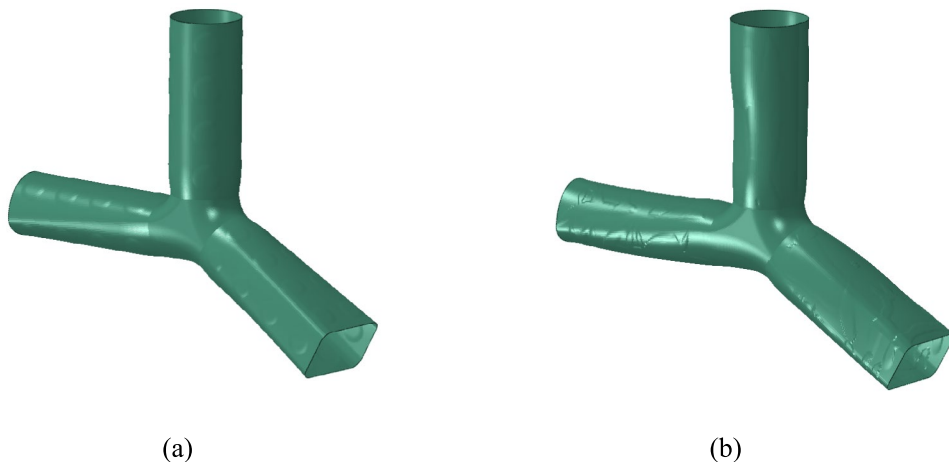
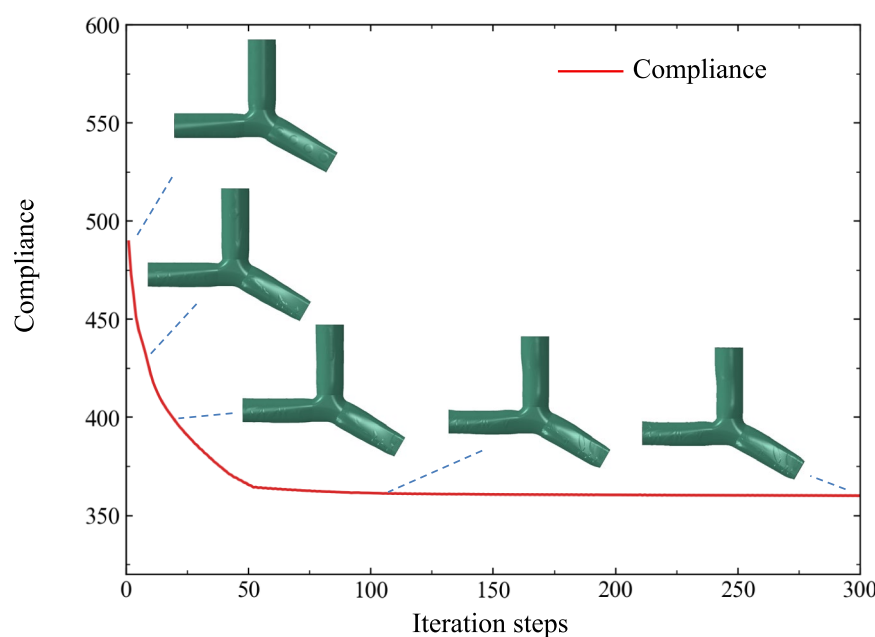
Fig. 23 Schematic illustration of the Tee-branch pipe shell structure. **a** Boundary condition. The shell thickness is set to 0.1. **b** The decomposed simple surfaces and their dimensional parameters. Currently, the structural compliance is 557.18

localized modifications enhance the overall structural stiffness. Although this example features nontrivial structural characteristics, the application of the multi-patch stitching scheme further demonstrates the effectiveness of the proposed algorithm in handling complex shell structures.

6 Conclusions

This study proposes a novel shape optimization method for thin-shell structures, integrating the advantages of CAD-based and node-based approaches. By leveraging the moving morphable components method and computational conformal mapping technique, the proposed method enables efficient shape optimization of complex shell geometries. The construction of a NURBS-based shape space allows global shape modifications with a set of control

Fig. 24 Iteration histories and intermediate results of the Tee-branch pipe shell structure. **a** Initial design ($C = 489.46$). **b** Final design ($C = 360.18$)



parameters while still being compatible with mesh-based nodal representation. The embedded shape component description facilitates the incorporation of local shape variations on general curved surfaces. Additionally, the introduction of the topology description function (TDF) and enhanced spline-based components enables the method to capture intricate local geometries accurately.

The hierarchical shape optimization framework allows for simultaneous global and local shape modifications, significantly expanding the design space and enhancing the structural representation. Furthermore, the surface cutting operation and multi-patch stitching scheme extend the method's applicability, enabling it to handle a broader range of complex shell structures. Numerical examples demonstrate the effectiveness of the proposed algorithm in improving structural stiffness. By integrating CAD-based optimization technique with the MMC framework, the

method achieves rapid convergence with fewer iterations and reduced design variables.

In the future, the proposed method can be extended to address other optimization objectives, including natural frequency maximization, buckling resistance, and stress minimization. Furthermore, incorporating manufacturing constraints into the optimization process presents a promising research direction, particularly for shell structures in sheet metal forming. Exploring draft angles, symmetry constraints, and other manufacturability conditions with shape optimization could lead to more practical and efficient co-design results.

Acknowledgements This work is supported by the National Key R&D Program of China (2022YFB3303000), the National Natural Science Foundation (12472344, 124B2042) and the Central Guiding Local Science and Technology Development Special Project of Liaoning Province (2024JH6/100700002).

Author contributions Chang Liu: Conceptualization, Methodology, Software, Writing, Supervision, Funding acquisition. Yanbo Ren: Software, Formal analysis, Data Curation, Writing—Original Draft. Shixin Zhao: Resources, Visualization. Xianglong Cao: Validation, Writing—Original Draft. Yinlin Guo: Software, Data Curation. Wending Huo: Methodology, Resources, Writing—Review & Editing. Xu Guo: Conceptualization, Project administration, Funding acquisition.

Funding The National Key R&D Program of China (2022YFB3303000), the National Natural Science Foundation (12472344, 124B2042) and the Central Guiding Local Science and Technology Development Special Project of Liaoning Province (2024JH6/100700002).

Data availability The data that support the findings of this study are available from the corresponding authors upon reasonable request.

Declarations

Conflict of interest The authors declare that they have no conflict of interest.

Replication of results All the key formulas for the calculation have been provided in the article. If the reader is interested, we can provide the calculation model.

References

- Afonso SMB, Hinton E (1995) Free vibration analysis and shape optimization of variable thickness plates and shells—I. Finite element studies. *Comput Syst Eng* 6:27–45. [https://doi.org/10.1016/0956-0521\(95\)00011-N](https://doi.org/10.1016/0956-0521(95)00011-N)
- Ansola R, Canales J, Tárrago JA, Rasmussen J (2002a) On simultaneous shape and material layout optimization of shell structures. *Struct Multidisc Optim* 24:175–184. <https://doi.org/10.1007/s00158-002-0227-x>
- Ansola R, Canales J, Tárrago JA, Rasmussen J (2002b) An integrated approach for shape and topology optimization of shell structures. *Comput Struct* 80:449–458. [https://doi.org/10.1016/S0045-7949\(02\)00019-6](https://doi.org/10.1016/S0045-7949(02)00019-6)
- Azegami H, Takeuchi K (2006) A smoothing method for shape optimization: traction method using the robin condition. *Int J Comput Methods* 03:21–33. <https://doi.org/10.1142/S0219876206000709>
- Azegami H, Wu ZC (1996) Domain optimization analysis in linear elastic problems: approach using traction method. *JSME Int J Ser A Mech Mater Eng* 39(2):272–278. https://doi.org/10.1299/jsmeia1993.39.2_272
- Bletzinger KU (2014) A consistent frame for sensitivity filtering and the vertex assigned morphing of optimal shape. *Struct Multidisc Optim* 49:873–895. <https://doi.org/10.1007/s00158-013-1031-5>
- Chapelle D, Bathe KJ (2011) The finite element analysis of shells—fundamentals. Computational fluid and solid mechanics. Springer, Berlin
- Chasapi M, Antolin P, Buffa A (2024) Fast parametric analysis of trimmed multi-patch isogeometric Kirchhoff-Love shells using a local reduced basis method. *Eng Comput* 40:3623–3650. <https://doi.org/10.1007/s00366-024-01980-6>
- Choi KK, Kim NH (2004) Structural sensitivity analysis and optimization 1: linear systems. Springer Science & Business Media
- Choi GPT, Leung LiuY GuX, Lui LM (2020) Parallelizable global conformal parameterization of simply-connected surfaces via partial welding. *SIAM J Imaging Sci* 13:1049–1083. <https://doi.org/10.1137/19M125337X>
- De Boor C (1972) On calculating with B-splines. *J Approx Theory* 6:50–62. [https://doi.org/10.1016/0021-9045\(72\)90080-9](https://doi.org/10.1016/0021-9045(72)90080-9)
- Espath LFR, Linn RV, Awruch AM (2011) Shape optimization of shell structures based on NURBS description using automatic differentiation. *Int J Numer Methods Eng* 88:613–636. <https://doi.org/10.1002/nme.3183>
- Falco SA, Afonso SMB, Vaz LE (2004) Analysis and optimal design of plates and shells under dynamic loads—I: finite element and sensitivity analysis. *Struct Multidisc Optim* 27:189–196. <https://doi.org/10.1007/s00158-003-0359-7>
- Fung Y (1977) A first course in continuum mechanics. Prentice-Hall, Englewood Cliffs
- Guo X, Zhang W, Zhong W (2014) Doing topology optimization explicitly and geometrically—a new moving morphable components based framework. *J Appl Mech* 81:081009. <https://doi.org/10.1115/1.4027609>
- Guo Y, Ye Q, Zheng X, Chen S, Lei N, Zhang Y, Gu D (2020) Computational generation and conformal fabrication of woven fabric structures by harmonic foliation. *Comput Methods Appl Mech Eng* 363:112874. <https://doi.org/10.1016/j.cma.2020.112874>
- Hirschler T, Bouclier R, Duval A, Elguedj T, Morlier J (2019) The embedded isogeometric Kirchhoff-Love shell: from design to shape optimization of non-conforming stiffened multipatch structures. *Comput Methods Appl Mech Eng* 349:774–797. <https://doi.org/10.1016/j.cma.2019.02.042>
- Hojjat M, Stavropoulou E, Bletzinger KU (2014) The vertex morphing method for node-based shape optimization. *Comput Methods Appl Mech Eng* 268:494–513. <https://doi.org/10.1016/j.cma.2013.10.015>
- Hughes TJR, Cottrell JA, Bazilevs Y (2005) Isogeometric analysis: CAD, finite elements, NURBS, exact geometry and mesh refinement. *Comput Methods Appl Mech Eng* 194:4135–4195. <https://doi.org/10.1016/j.cma.2004.10.008>
- Huo W, Liu C, Du Z, Jiang X, Liu Z, Guo X (2022) Topology optimization on complex surfaces based on the moving morphable component method and computational conformal mapping. *J Appl Mech* 89:051008. <https://doi.org/10.1115/1.4053727>
- Huo W, Liu C, Guo Y, Du Z, Zhang W, Guo X (2025) Explicit topography design for complex shell structures based on embedded spline components. *J Mech Phys Solids* 196:105974. <https://doi.org/10.1016/j.jmps.2024.105974>
- Jameson A, Vassberg JC (2000) Studies of alternative numerical optimization methods applied to the brachistochrone problem. *Comput Fluid Dyn J* 9(3):281–296
- Jiang X, Huo W, Liu C, Du Z, Zhang X, Li X, Guo X (2023) Explicit layout optimization of complex rib-reinforced thin-walled structures via computational conformal mapping (CCM). *Comput Methods Appl Mech Eng* 404:115745. <https://doi.org/10.1016/j.cma.2022.115745>
- Kang P, Youn SK (2015) Isogeometric analysis of topologically complex shell structures. *Finite Elem Anal des* 99:68–81. <https://doi.org/10.1016/j.finel.2015.02.002>
- Kang P, Youn SK (2016) Isogeometric shape optimization of trimmed shell structures. *Struct Multidisc Optim* 53:825–845. <https://doi.org/10.1007/s00158-015-1361-6>
- Kreisselmeier G, Steinhauser R (1980) Systematic control design by optimizing a vector performance index. In: Computer aided design of control systems. Elsevier, pp 113–117. <https://doi.org/10.1016/b978-0-08-024488-4.50022-x>
- Le C, Bruns T, Tortorelli D (2011) A gradient-based, parameter-free approach to shape optimization. *Comput Methods Appl Mech Eng* 200:985–996. <https://doi.org/10.1016/j.cma.2010.10.004>

- Lee H, Seo H, Park GJ (2003) Design enhancements for stress relaxation in automotive multi-shell-structures. *Int J Solids Struct* 40:5319–5334. [https://doi.org/10.1016/S0020-7683\(03\)00291-9](https://doi.org/10.1016/S0020-7683(03)00291-9)
- Lui LM, Lam KC, Wong TW, Gu X (2013) Texture map and video compression using beltrami representation. *SIAM J Imaging Sci* 6:1880–1902. <https://doi.org/10.1137/120866129>
- Lui LM, Lam KC, Yau ST, Gu X (2014) Teichmuller mapping (T-Map) and its applications to landmark matching registration. *SIAM J Imaging Sci* 7:391–426. <https://doi.org/10.1137/120900186>
- Meng TW, Choi GPT, Lui LM (2016) TEMPO: feature-endowed teichmüller extremal mappings of point clouds. *SIAM J Imaging Sci* 9:1922–1962. <https://doi.org/10.1137/15M1049117>
- Najian Asl R, Bletzinger KU (2023) The implicit bulk-surface filtering method for node-based shape optimization and a comparison of explicit and implicit filtering techniques. *Struct Multidisc Optim* 66:111. <https://doi.org/10.1007/s00158-023-03548-2>
- Nørtoft P, Gravesen J (2013) Isogeometric shape optimization in fluid mechanics. *Struct Multidisc Optim* 48:909–925. <https://doi.org/10.1007/s00158-013-0931-8>
- Park BU, Seo YD, Sigmund O, Youn SK (2013) Shape optimization of the stokes flow problem based on isogeometric analysis. *Struct Multidisc Optim* 48:965–977. <https://doi.org/10.1007/s00158-013-0939-0>
- Piegl L, Tiller W (2012) The NURBS book. Springer Science & Business Media
- Pinkall U, Polthier K (1993) Computing discrete minimal surfaces and their conjugates. *Exp Math* 2:15–36
- Qian X (2010) Full analytical sensitivities in NURBS based isogeometric shape optimization. *Comput Methods Appl Mech Eng* 199:2059–2071. <https://doi.org/10.1016/j.cma.2010.03.005>
- Radtke L, Bletsos G, Kühl N, Suchan T, Rung T, Duster A, Welker K (2023) Parameter-free shape optimization: various shape updates for engineering applications. *Aerospace* 10:751. <https://doi.org/10.3390/aerospace10090751>
- Rian IM, Sassone M, Asayama S (2018) From fractal geometry to architecture: designing a grid-shell-like structure using the Takagi-Landsberg surface. *Comput-Aided des* 98:40–53. <https://doi.org/10.1016/j.cad.2018.01.004>
- Samareh JA (2001) Survey of shape parameterization techniques for high-fidelity multidisciplinary shape optimization. *AIAA J* 39:877–884. <https://doi.org/10.2514/2.1391>
- Schmöld D, Devresse B, Geiser A, Bletzinger KU (2025) Simultaneous node-based shape and thickness optimization of thin-walled structures using the explicit vertex morphing method. *Struct Multidisc Optim* 68:37. <https://doi.org/10.1007/s00158-025-03977-1>
- Sigmund O (1994) Design of material structures using topology optimization. Ph.D. thesis, Technical University of Denmark Lyngby
- Suarez Espinoza PA, Bletzinger KU, Hörnlein HREM, Daoud F, Schuhmacher G, Klug M (2012) Shape optimisation in the design of thin-walled shells as components of aerospace structures. *Aeronaut J* 116:793–814. <https://doi.org/10.1017/S0001924000007284>
- Svanberg K (1987) The method of moving asymptotes—a new method for structural optimization. *Int J Numer Methods Eng* 24:359–373. <https://doi.org/10.1002/nme.1620240207>
- Swartz KE, Mittal K, Schmidt M, Barrera JL, Watts S, Tortorelli DA (2023) Yet another parameter-free shape optimization method. *Struct Multidisc Optim* 66:245. <https://doi.org/10.1007/s00158-023-03684-9>
- Talebitooti R, Zarastvand MR (2018) The effect of nature of porous material on diffuse field acoustic transmission of the sandwich aerospace composite doubly curved shell. *Aerospace Sci Technol* 78:157–170. <https://doi.org/10.1016/j.ast.2018.03.010>
- Taubin G (1995) Estimating the tensor of curvature of a surface from a polyhedral approximation. In: Proceedings of IEEE international conference on computer vision. IEEE Comput. Soc. Press, Cambridge, pp 902–907
- Träff EA (2023) Efficient methods for high fidelity topology optimization. Ph.D. thesis, Technical University of Denmark Lyngby
- Vu Bac N, Duong TX, Lahmer T, Sauer RA, Park HS, Rabczuk T (2018) A NURBS-based inverse analysis for reconstruction of nonlinear deformations of thin shell structures. *Comput Methods Appl Mech Eng* 331:427–455. <https://doi.org/10.1016/j.cma.2017.09.034>
- Wall WA, Frenzel MA, Cyron C (2008) Isogeometric structural shape optimization. *Comput Methods Appl Mech Eng* 197:2976–2988. <https://doi.org/10.1016/j.cma.2008.01.025>
- Wang Y, Wang S, Zhang L, Zhao B (2003) Shape control of Bézier surfaces with iso-parametric monotone curvature constraints. *Comput Aided Geom Des* 20:383–394. [https://doi.org/10.1016/S0167-8396\(03\)00080-3](https://doi.org/10.1016/S0167-8396(03)00080-3)
- Wang Y, Wang Z, Xia Z, Hien Poh L (2018) Structural design optimization using isogeometric analysis: a comprehensive review. *Comput Model Eng Sci* 117:455–507. <https://doi.org/10.31614/cmes.2018.04603>
- Yu YY, Lin Y, Chen M, Li K (2015) A new method for ship inner shell optimization based on parametric technique. *Int J Nav Archit Ocean Eng* 7:142–156. <https://doi.org/10.1515/ijnaoe-2015-0011>
- Zhang W, Yuan J, Zhang J, Guo X (2016) A new topology optimization approach based on moving morphable components (MMC) and the ersatz material model. *Struct Multidisc Optim* 53:1243–1260. <https://doi.org/10.1007/s00158-015-1372-3>

Publisher's Note Springer Nature remains neutral with regard to jurisdictional claims in published maps and institutional affiliations.

Springer Nature or its licensor (e.g. a society or other partner) holds exclusive rights to this article under a publishing agreement with the author(s) or other rightsholder(s); author self-archiving of the accepted manuscript version of this article is solely governed by the terms of such publishing agreement and applicable law.